Atomic, Radiation, and Hydrodynamics Modeling in Support of the Sandia Light Ion Beam Program

D.H. Cohen, H.K. Chung,
P. Wang, J.J. MacFarlane

May 1998

UWFDM-1074

FUSION TECHNOLOGY INSTITUTE

UNIVERSITY OF WISCONSIN

MADISON WISCONSIN

Atomic, Radiation, and Hydrodynamics Modeling in Support of the Sandia Light Ion Beam Program

D. H. Cohen, H. K. Chung, P. Wang, and J. J. MacFarlane

Fusion Technology Institute
University of Wisconsin–Madison
1500 Engineering Dr.
Madison, Wisconsin 53706

May 1998

UWFDM-1074

We dedicate this work to the memory of our friend and colleague, Alex Filuk.

Contents

1. Introduction

The purpose of this report is to summarize work performed by the University of Wisconsin during the period July 1996 through June 1997 in support of the light ion beam fusion program at Sandia National Laboratory. This work involved both modeling and data analysis, and three separate efforts focused on the ion source generation and the beam interactions with the argon gas cell are detailed here. These efforts involved the continued use of hydrodynamic, radiative, and atomic modeling codes that have been developed over the years at the University of Wisconsin in order to model Sandia light ion beam experiments, among others. Additionally, we have developed new codes specifically for the work described in this report. These new codes include an atomic and radiation transfer model of the LIBORS process and a multiparameter, multi-line spectral fitting code. We have constructed detailed atomic models of argon, lithium, and silver for these calculations.

Table 1.1. Tasks for Fiscal Year 1997

1. Analyze and model argon gas cell spectra to evaluate diagnostics of thermal electron and line opacity properties.
2. Model LIBORS process to reproduce time-dependent ionization properties of lithium plasma irradiated with a tuned dye laser.
3. Model formation and expansion of lithium ion beam source plasma to benchmark spectral diagnostics and explore sensitivities to, e.g., laser pulse characteristics.
4. Provide atomic files for use in PIC code.
5. Detail ion beam stopping power analysis.
6. Document results to Sandia National Lab in report(s).

The tasks described in this report are summarized in Table 1.1. They all involve the analysis and modeling of experimental results from investigations of various aspects of light ion beam generation and propagation carried out at SNL over the past few years. The work

described in § 2 includes the analysis of experimental data taken in 1994 from PBFA-II beam interactions with an argon gas cell. The purpose of these experiments was to characterize the gas cell properties based on observations of time-dependent optical spectra from the Ar. The LIBORS and lithium ion source modeling (§ 3 and § 4 respectively) involve attempts to understand the creation and time-dependent behavior of a lithium plasma in light-lab experiments carried out over the past two years. These experiments did not involve PBFA-II ion beams, but rather they employed one or two separate lasers to generate a plasma from a LiAg coupon in the light-lab. This plasma was observed with time-resolved spectroscopy in order to characterize its ionization and density. The results from these experiments and modeling can help to better generate an ion source on PBFA-II.

Additionally, we provided atomic data files (argon, thus far) to Dale Welch for use in PIC code simulations. We completed the ion stopping power analysis, delivered the code to SNL, and submitted a paper to *Physics of Plasmas*.

The first section of the report describes our effort to analyze optical spectra from argon gas cell ion beam experiments and then to model the ionization/excitation dynamics of the argon. Optical spectra containing many Ar features were analyzed with an empirical spectral model that included opacity broadening along with other line-broadening mechanisms. The spectral features were fit simultaneously, with fluxes, optical depths, and electron densities (from Stark widths) derived for each fit. Equally important was the derivation of confidence limits on these parameters. We determined these using the correct formalism for joint probability distributions. The ranges determined from the line fitting were compared with self-consistent models of the excitation/ionization dynamics in the Ar gas cell. These models include the effects of non-thermal electrons produced by the ion beam and direct ionization/excitation by the ion beam itself. We will explore in future work the possibility of using the spectral characteristics as beam property diagnostics.

The next section covers our modeling of the LIBORS (Laser Ionization Based On Resonance Saturation) process. These experiments use a dye laser tuned to the Li I $2s - 2p$ resonance transition at 6807 Å to excite, and then ionize lithium that has already been vaporized by a separate laser pulse. LIBORS is promising because it has the desirable property of being able to ionize the lithium quickly and efficiently with a minimum of heating. Our modeling effort here includes a calculation of a detailed atomic model for lithium, including the two-photon ionization rate from the $2p$ level of Li I. We employed this model in a both a zero- and one-dimensional radiation transfer and collisional-radiative calculation of the ionization/excitation dynamics of the lithium vapor in order to test the sensitivity to the laser intensity and gas density.

The final section describes our initial efforts to model the time-dependent behavior of the lithium-silver ion source as it is generated by the laser heating of a LiAg coupon. This effort was initially undertaken in order to generate realistic temperature and density profiles to be used as input for the LIBORS modeling; however, its utility may prove to be broader than that, as it now appears that the dye laser need not necessarily be employed in the generation of the lithium ion source. The purpose of this modeling is twofold: it can be used to interpret the time- and space-dependent spectra of the ion source in order to characterize its properties, and it also can be used to study the sensitivity of the ion source properties to various physical parameters, so that the source can be optimized for beam generation.

2. Analysis and Modeling of Line-broadened Ar II Spectra Obtained from Ion Beam Transport Experiments

Spectra collected when the PBFA-II light ion beam has been passed through an argon gas cell have the potential to provide many useful diagnostics of the gas cell properties, including possibly the properties of non-thermal particles as well. In this section we describe the modeling carried out at the University of Wisconsin of argon gas cell spectra taken over the past several years at Sandia. One of our goals has been to include enough detailed atomic physics to make quantitative spectral models which can be used to reproduce the experimental data well enough to constrain T_e and n_e as a function of time. This initially has lead us to investigate the importance of opacity broadening in the Ar II optical spectra and its influence on the n_e determinations.

The bulk of the work reported here involves our development of a statistical method for analyzing multi-line spectra that include opacity broadened features in such a way as to place firm statistical limits on the properties of individual lines (optical depths) as well as global properties (electron densities and temperatures). We also report on our initial attempts to reproduce these properties using a detailed atomic model of argon, in conjunction with a time-dependent collisional-radiative (CR) calculation that includes the effects of hot electrons and beam ions.

2.1. Background

Electron densities in the argon gas cell experiments were initially determined from Stark widths, which were based on the results of fitting the observed emission lines with ROBFIT. This code assumes that lines are completely optically thin, and then fits a mathematical model to the line shape. The densities measured in this way were higher than the predictions of both the IPROP PIC code [1], and our collisional-radiative calculations. It is possible that the walls or the ion diode region are sources of additional electrons in the

experiment which is not accounted for in these codes. However, it is also possible that the emission lines in the data are optically thick, and therefore attributing their widths entirely to Stark broadening has lead to an overestimate of the electron density.

Spectral lines always have finite widths, due to finite lifetimes of atomic states (natural broadening), plasma interactions (collisional broadening), or thermal motions of emitting atoms (Doppler broadening). Collisional broadening (or Stark broadening for ion-dominated plasma) has been a key mechanism to determine electron densities because the line width is proportional to the rate of collisions. Doppler broadening, on the other hand, is generally useful for the determination of ion temperatures. Note that there are other types of collisional broadening (see e.g. [2]), but we find Stark broadening to be the dominant collisional broadening mechanism in this work.

In addition to these broadening mechanisms, which depend on the atomic-scale physics of the plasma, one must consider opacity broadening, which depends on the global plasma properties and the observer's line of sight via the total line optical depth. Opacity broadening arises due to the fact that photons near line center are absorbed with higher probabilities than photons in the line wings. As a result, photon intensities near line center saturate once a line becomes optically thick, but intensities in the line wings continue to grow with increasing optical depth. Lines that are dominated by opacity broadening have flat-topped profiles, and are much broader than optically thin lines.

The effect of opacity on line shapes can be seen in the following formalism.

The transport equation for radiation intensity I_ν at a frequency ν along a line of sight s is written as

$$\frac{dI_\nu}{ds} = \eta_\nu - \chi_\nu I_\nu,$$

where η_ν is an emissivity and χ_ν is an absorption coefficient, or opacity. In a two-level atom, they are written in terms of upper and lower level population densities, n_u, n_l, an absorption

oscillator strength f_{lu}, or spontaneous decay rate A_{lu}, and an intrinsic absorption profile ϕ_ν,

$$\eta_\nu = n_u A_{lu} \frac{h\nu}{4\pi} \phi_\nu = n_u \left(\frac{2h\nu^3}{c^2} \right) \left(\frac{\pi e^2}{mc} \right) f_{lu} \phi_\nu$$

$$\chi_\nu = \left[n_l - \frac{g_l}{g_u} n_u \right] \left(\frac{\pi e^2}{mc} \right) f_{lu} \phi_\nu .$$

The intrinsic absorption profile may account for natural, Stark, or Doppler broadening, but not opacity or instrumental broadening.

The radiation transport equation can be written in terms of optical depth τ_ν and source function S_ν,

$$\frac{dI_\nu}{d\tau_\nu} = I_\nu - S_\nu ,$$

where

$$d\tau_\nu = -\chi_\nu ds$$

$$S_\nu = \frac{\eta_\nu}{\chi_\nu} ,$$

and s is the path length.

If S_ν is uniform in space, then the emergent intensity I_ν from a medium of an optical depth τ_ν can be written as

$$I_\nu = S_\nu \left(1 - e^{-\tau_\nu} \right) .$$

If τ_ν is much less than unity, I_ν will be simply the source function S_ν times optical depth τ_ν,

$$I_\nu \sim S_\nu \tau_\nu = \eta_\nu l = n_u A_{lu} \frac{h\nu}{4\pi} \phi_\nu l$$

where l is the length along a line of sight. In this case, of course, opacity broadening is unimportant, and the line shape is described by ϕ_ν. If τ_ν is much larger than unity, then the intensity approaches the source function (Planck function when plasma is in LTE) at any

frequency where $\tau_\nu \gg 1$, leading to a flat-topped profile. Opacity effects on line broadening of three lines are illustrated in Figure 2.1.

It is important to note that not only line widths but also peak intensities are dependent on opacity. The peak intensity increases with optical depth until it becomes optically thick and saturates at the source function. As the opacity is increased further, points on the wings become optically thick, and those points also saturate, broadening the flat peak of the line, but not increasing the peak intensity. For a pair of optically thin lines with the same lower level, the line-center intensity ratio reflects the optical depth ratio. For example, in one of our models, the ratio of optical depths between 4348 Å and 4352 Å is approximately 20 if they are statistically populated, and the ratio of the optical depths is reflected in the intensity ratios,

$$\frac{I_{4348}}{I_{4352}} = \frac{S_{4348}\tau_{4348}}{S_{4352}\tau_{4352}} \sim \frac{\tau_{4348}}{\tau_{4352}} \sim 20.$$

If, however, one of the lines is optically thick but the other is not, then the line ratio no longer reflects the relative optical depths. For example, if τ_{4348} is 10 and τ_{4352} is 0.5, then the ratio between peak intensities will be

$$\frac{I_{4348}}{I_{4352}} = \frac{S_{4348}\left(1 - e^{-\tau_{4348}}\right)}{S_{4352}\left(1 - e^{-\tau_{4352}}\right)} \sim \frac{S_{4348}}{S_{4352}\tau_{4352}} \sim 2.$$

This effect is shown in Figure 2.2. In this case, the line shape will provide information about the optical depth, but only if opacity broadening dominates other broadening mechanisms.

It should be noted that, as a consistency check, optical depth information also can be inferred from determinations of level populations and ion densities integrated over sight-lines in the emitting plasma. A robust method of spectral analysis will therefore combine simultaneous fits to many lines, both thin and thick, in order to develop a consistent picture of optical depths, level populations, and densities.

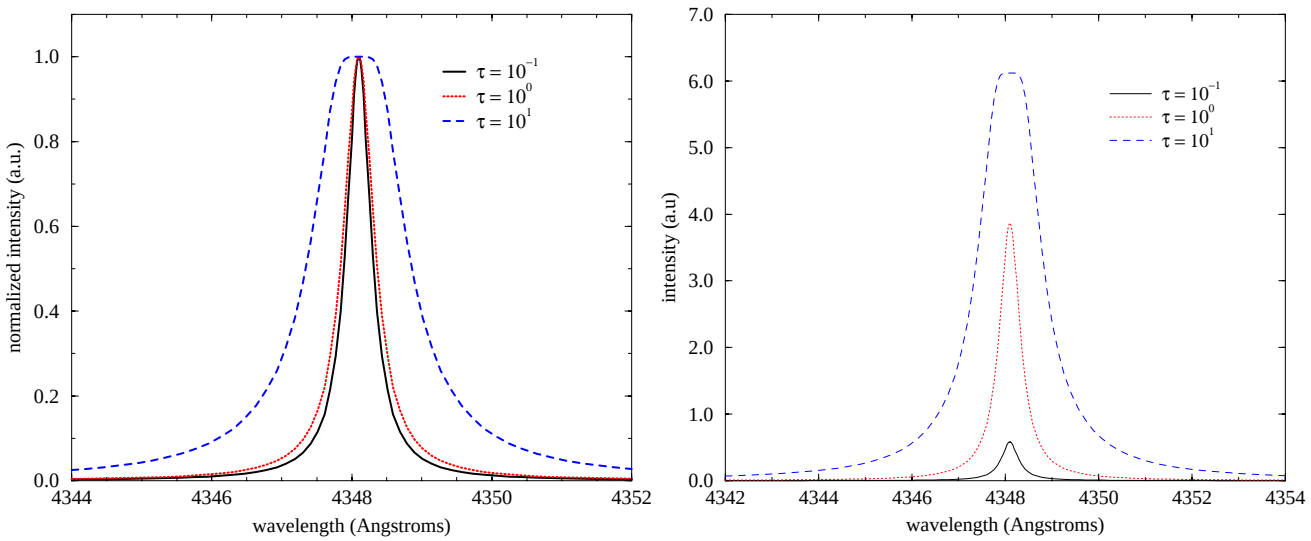

Figure 2.1. We show three idealized line profiles, having different total line optical depths. In the panel on the left we scale the lines so that their peaks have the same value. The effect of opacity on line shape can be clearly seen. In the panel on the right the lines are unscaled and the effect of opacity on peak intensity can also be seen.

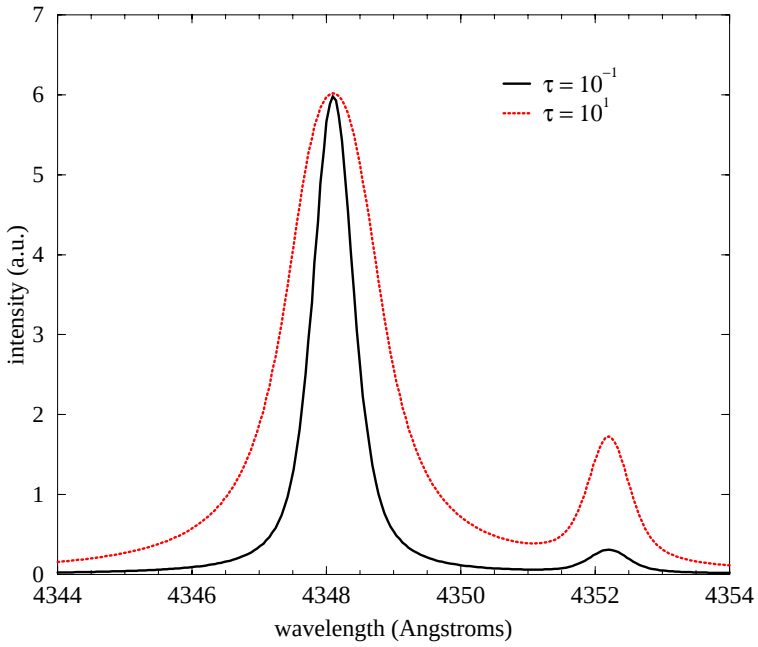

Figure 2.2. Line profiles for 4348, 4352 Å in the case where 4348 Å is optically thin (black) and optically thick (red). The lines have an optical depth ratio of 20, which is reflected in the line ratio only in the optically thin case.

Finally, one must consider the effects of instrumental broadening upon line profiles. Every instrument has a response function that has a finite width, the effect of which is to convolve the intrinsic line profile with some instrumental broadening function. Because of the difficulty of deconvolution and the errors involved, it is advisable to treat the effect of the instrumental profile as another broadening mechanism to be applied to calculated line profiles before they are compared to data. Instrumental broadening can smooth the idealized flat-topped profiles of optically thick lines, as shown in Figure 2.3, where an instrumental FWHM = 0.5 Å was assumed.

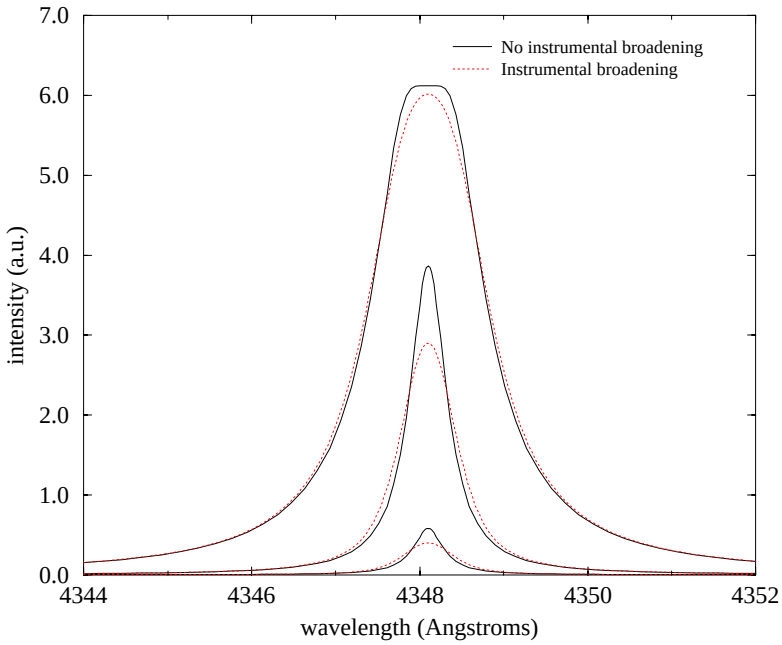

Figure 2.3. Three pairs of line profiles are shown; each pair contains an intrinsic line profile and the same profile convolved with an instrumental response function. The optically thin profile (bottom) has the largest relative effect, but the optically thick profile (top) is affected too, as the instrumental broadening causes it to lose its flat-topped morphology.

2.2. Spectral Analysis Program

In order to analyze spectral data taken from PBFA-II Ar gas cell experiments, we have developed a line profile fitting code, MSPECT. This code fits a line profile model that includes natural, Doppler, Stark, opacity, and instrumental broadening to a series of spectral lines. There are four adjustable parameters: T, n_e, τ (of a single reference line), and the FWHM of the instrumental response. The level populations giving rise to each line are tied together via the assumption of LTE. The optical depths of each line are tied to the optical depth of the 4348 Å line.

For a given value of the electron density parameter, a line-shape function is calculated assuming a Stark width given in reference [3], which we list in Table 2.1. In practice, we calculate the intrinsic line profile using a Voigt function, then solve the radiation

transport (which further broadens optically thick lines), and finally convolve the line profile with an instrumental response function, which we take to be Gaussian.

Table 2.1. Stark Width Values for Ar II Lines

Line Wavelength (Å)	Half-Width[a] (Å)
4331.20	0.338
4332.03	0.320
4337.07	0.320
4348.06	0.292
4352.20	0.350
4362.07	0.320
4367.80	0.320
4370.75	0.320
4371.33	0.324
4374.86	0.320
4375.95	0.244
4379.67	0.316

[a] The values are for $n_e = 10^{17}$ (cm^{-3}) taken from reference [3]. For lines not included in this reference, we adopt the value of 0.32 Å.

The best-fit model parameters are determined using a Levenberg-Marquardt minimization technique based on the χ^2 statistic [4]. In this method, the N-dimensional parameter space is searched for the global minimum of the χ^2 function,

$$\chi^2 = \sum \frac{(x_i - m_i)^2}{\sigma_i^2}.$$

Local minima are found by the evaluation of partial derivatives of the model function with respect to the free parameters. After the program converges on a local minimum, the parameters are given a random adjustment, and a new local minimum is sought. When this process is repeated a specified number of times and fails to reduce the value of the χ^2 statistic, the local minimum with the smallest χ^2 value is taken to be the global minimum. In order to evaluate the errors on the derived parameters, we use the $\Delta\chi^2$ statistic for joint

probability distributions [5]. In this method, $\Delta\chi^2 = \chi^2 - \chi^2{}_{min}$ is defined on a regular grid in the N-dimensional parameter space centered on the best-fit point.

Confidence limits of a given level are based on values of $\Delta\chi^2$, and any portion of parameter space that lies within the contour corresponding with the specified value is said to contain the true solution with the given confidence. The $\Delta\chi^2$ values that correspond to a given confidence level increase with increasing numbers of free parameters (but see reference [6]). The FWHM of the instrumental response was allowed to be a free parameter within the range 0.4 Å $<$ FWHM $<$ 0.5 Å. We found that the actual value does not substantially affect the solution.

The temperature is known to within a factor of two, and we fit the data using one of several fixed temperatures (between 2 and 3 eV). The primary parameter values of interest are the optical depth and the electron density. These two parameters tend to be anticorrelated, because they both increase with increasing line width. We therefore use the $\Delta\chi^2$ values for two parameters of interest (2.30 for 68% and 4.61 for 90%) in the rest of this section.

We performed several tests of the fitting program that involved generating artificial data sets from our line profile model and adding Poisson noise. We then used the fitting program to see how reliably we could recover the true parameters. We did tests with only one parameter free (in which the original values were very accurately recovered), as well as tests with all four parameters free. For the same statistical error on the data, there were significantly larger errors on the parameter values in the cases with multiple free parameters. But in all cases, the true values in the simulations lay within the 99% confidence limits of the fits to the simulated data.

We also tested the performance of the code with different numbers of lines. We found that the more lines that were included, the smaller the solution space and the better

we were able to reproduce the true parameters. This result is expected, however, when the model is perfectly known and the formal errors are exact representations of the uncertainty in the data, as is the case in these simulations. With real data, considering additional lines that might contain blends, or have errors in their f-values, may bias the fit. Finally, we simulated data with a finite, noisy continuum. We found good results both when we fit the continuum as an additional component of the model, and when we fit and subtracted it before analyzing the lines. Ultimately, we decided to fit and subtract the continuum first. This aspect of the analysis is also bound to be affected by unaccounted for sources of error.

Before fitting the data, we made small adjustments to the assumed line center wavelengths. These values were determined by fitting profiles to individual lines, one at a time, and then using the best fit values in the global MSPECT fit. There were several line blends in the data. For these features we first fit the features individually, allowing the difference in wavelength between the two blended lines to be a free parameter in order to determine the optimal line-center wavelengths to use for each component.

We censored any points near the line wings that might stem from unidentified blends, and fit up to 12 emission lines simultaneously, using statistical uncertainties determined from photon counts assuming Poisson noise. The global minimum thus found was then used as the ${\chi^2}_{best}$ in the $\Delta\chi^2$ calculation to assess the uncertainties on the fitted parameters, τ and n_e.

2.3. Results

Here we present the results of our fitting program for five data sets from shot number 6022, $t1r.ufo$ – $t5r.ufo$, taken between 10 ns and 22 ns. These data were recorded with a 2400 lines mm^{-1} grating, giving a spectral resolution of 0.5 Å or better. In Table 2.2 we list the lines that were included in this analysis. Note that there are several blends in the data.

Table 2.2. Ar II Lines Used for Fitting

Wavelength (Å)	Lower Level	Upper Level	f-value[a]	gf
4331.20[b]	$4s\ ^4P$	$4p\ ^4P$	0.166	0.664
4332.03[b]	$3d\ ^4D$	$4p\ ^4P$	0.023	0.092
4337.07	$4p\ ^2P$	$5s\ ^2D$	0.065	0.260
4348.06	$4s\ ^4P$	$4p\ ^4D$	0.483	2.898
4352.20	$3d\ ^4D$	$4p\ ^4P$	0.058	0.116
4362.07	$3d\ ^2D$	$4p\ ^2D$	0.026	0.104
4367.80	$4s\ ^2S$	$5p\ ^2P$	0.013	0.026
4370.75[c]	$3d\ ^2D$	$4p\ ^2D$	0.196	0.784
4371.33[c]	$3d\ ^4D$	$4p\ ^4P$	0.041	0.246
4374.86	$4p\ ^2P$	$5s\ ^2P$	0.047	0.188
4375.95	$4s\ ^2P$	$4p\ ^2S$	0.030	0.120
4379.67	$4s\ ^4P$	$4p\ ^4D$	0.307	0.614

[a] The f-values are from [3].
[b,c] These line pairs are blended in the data.

Electron densities had been derived from the Stark widths of the 4348 Å line using ROBFIT, assuming no opacity broadening [1]. As a consistency check, we fit these same data using MSPECT with a model constrained to be optically thin. As shown in Table 2.3, for the 4348 Å line we derived densities consistent with those made using ROBFIT.

Table 2.3. 4348 Å Line-Width Comparison and Optically Thin Analysis

File	Time	ROBFIT		MSPECT
		4348 Å Line Width	n_e	n_e
	(ns)	(Å)	(10^{17} cm^{-3})	(10^{17} cm^{-3})
$t1$	10	$0.86 \pm .13$	1.75	1.93
$t2$	13	$0.86 \pm .05$	1.75	1.69
$t3$	16	$1.06 \pm .04$	2.56	2.45
$t4$	19	$1.30 \pm .05$	3.47	3.49
$t5$	22	$1.51 \pm .07$	4.16	4.10

If the lines are optically thin, and if the populations are in LTE, then we should be able to fit all the data with a single model, in which line intensities are controlled by

the electron temperature via the level populations and line widths are controlled by the electron density via Stark broadening. To test this, we used MSPECT to fit the entire spectrum simultaneously with a completely optically thin model normalized to the 4348 Å line. As can be seen in Figure 2.4, the fits to the lines other than 4348 Å are generally bad, both from the point of view of normalization and of line-widths. The fact that the model underestimates the fluxes of the weaker lines when it matches the strong 4348 Å line is an indication that we may be neglecting opacity effects (see Figure 2.2 for a demonstration of the effect of optical depth on line ratios).

We next fit each of the five data sets with an optically *thick* MSPECT model. The optical depth, and hence level population, is fit for the 4348 Å line, and the optical depths for all the other lines are determined from the 4348 Å line assuming LTE at a temperature of 2.5 eV. We also fit the data assuming temperatures of 2 and 3 eV, but found little sensitivity to the temperature in this range. The electron density was fit from the Stark broadening, and a single value of electron density was assumed for all lines. In Figure 2.5 we show the data again with the best-fit optically thick models. It can clearly be seen that this fit is much better than that for the optically thin model. This is quantified in Table 2.4, where we compare the overall reduced χ^2 statistic for each of the five data sets and the two different types of models.

Table 2.4. Fit Statistics for Optically Thin and Optically Thick Models

File	Time (ns)	Optically Thin χ^2_ν	Optically Thick χ^2_ν
$t1$	10	3.2	1.1
$t2$	13	7.9	1.6
$t3$	16	17.1	2.2
$t4$	19	14.6	1.4
$t5$	22	8.7	1.2

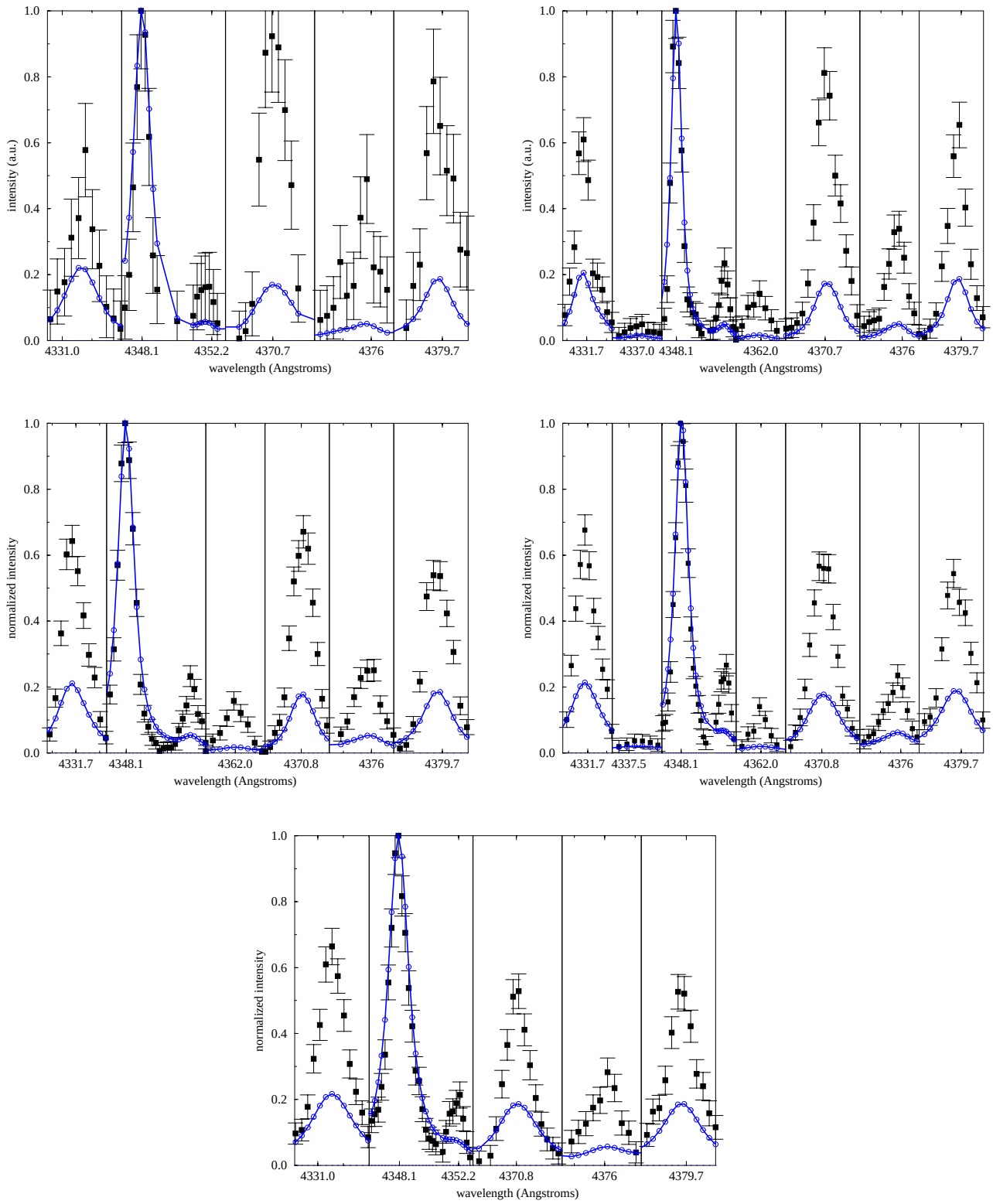

Figure 2.4. The five data sets, $t1r.ufo$ (top left) – $t5r.ufo$ (bottom), are shown in black with statistical errors. The best fit, optically *thin* MSPECT model is shown in blue.

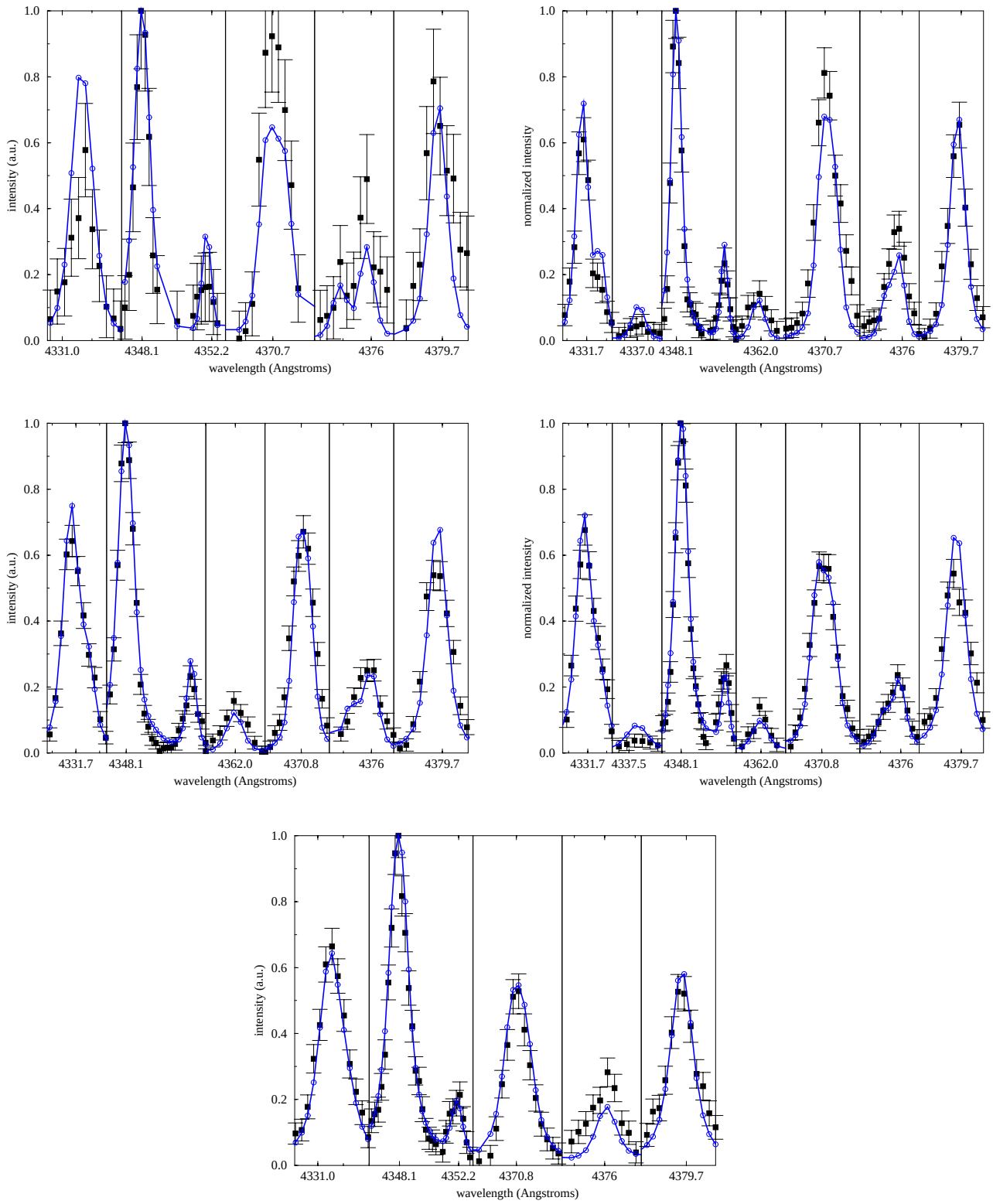

Figure 2.5. The five data sets, $t1r.ufo$ (top left) – $t5r.ufo$ (bottom right), are shown in black with statistical errors. The best fit, optically *thick* MSPECT model is shown in blue.

The earliest data set, $t1r.ufo$, actually has the best χ^2 statistic, due to its relatively large formal uncertainties. Even though the model lies closer to the data in subsequent data sets, the fits are formally worse because of the smaller statistical errors. The reduced χ^2 values for these later shots are slightly larger than would be expected for formally good fits, although they are significantly better than the optically thin fits. This is most likely due to systematic and unaccounted for statistical errors, which will be discussed below.

From the best-fit optically thick model we have determined electron densities and optical depths for the five different data sets. These fits correspond with the models indicated in black in Figure 2.5. The best fit values and the formal uncertainties (extent of the 90% confidence limits) are listed in Table 2.5. The solution spaces indicated by the 90% confidence limits are shown in Figure 2.6. Note the anti-correlation between the two parameters. It was for this reason that we used the formalism for joint-probability distributions [5].

Table 2.5. Fitted Parameters from Optically Thick Model

$File$	$n_e/10^{17}$ (cm^{-2})	τ_{4348}	τ_{4352}	τ_{4362}	τ_{4376}	τ_{4380}
$t1r(10ns)$	$0.50^{+0.30}_{-0.22}$	$24.9^{+26}_{-10.8}$	1.24	0.37	0.82	4.97
$t2r(13ns)$	$0.49^{+0.08}_{-0.10}$	$20.5^{+6}_{-3.5}$	1.07	0.31	0.67	4.11
$t3r(16ns)$	$0.68^{+0.08}_{-0.04}$	$17.5^{+1.8}_{-2.7}$	0.88	0.26	0.58	3.50
$t4r(19ns)$	$1.22^{+0.12}_{-0.10}$	$10.5^{+1.2}_{-1.45}$	0.52	0.16	0.34	2.09
$t5r(22ns)$	$1.75^{+0.20}_{-0.16}$	$6.7^{+1.2}_{-0.9}$	0.34	0.10	0.23	1.38

The main result of this model fitting is that including opacity effects greatly improves the model fits. It also decreases the electron density values with respect to the optically thin case, in which the deconvolved widths were assumed to be dominated by Stark broadening. This change is due to the fact that some of the lines have significant optical depths. This is especially true for the 4348 Å and 4380 Å lines. The significance of these results will be discussed in the following subsection. However, first we will briefly discuss the sources of error and uncertainty in the optically thick modeling of the data.

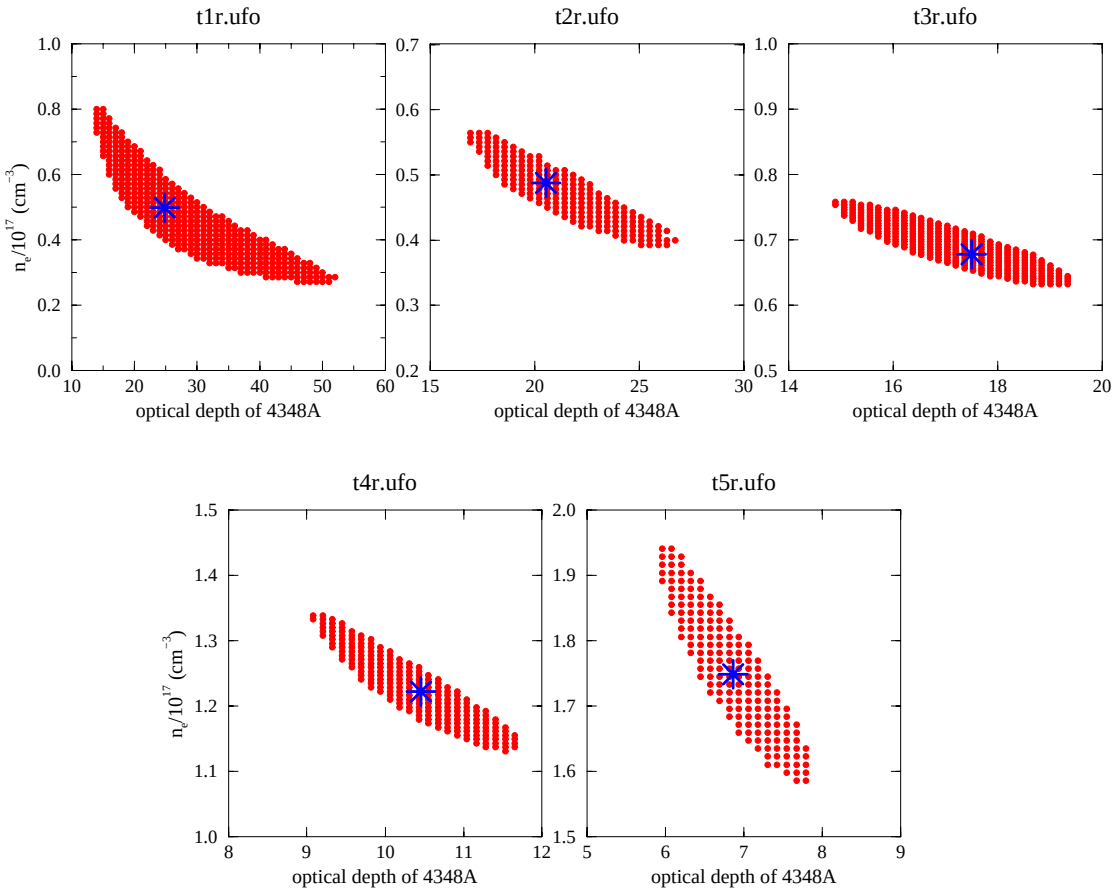

Figure 2.6. The confidence limits on the electron density and 4348 Å optical depth are shown for the fits to each of the five data sets. The red regions indicate the 90% confidence limits and the blue asterisks mark the best fit parameters. Note that the values of n_e and τ are strongly anti-correlated.

The χ^2_ν values for the optically thick model fits to the five data sets are significantly better than those for the optically thin model, but they are about 50 percent larger than would be expected for formally good fits. For a model fit to give a $\chi^2_\nu \approx 1$, the statistical uncertainties must be properly accounted for. In our analysis, we have used statistical uncertainties that are based on the finite signal-to-noise of the data. However, there are other sources of (mostly systematic) error which we have not formally accounted for. We will now evaluate these:

(1) LTE assumptions

Our model assumes that all levels are in LTE. However, there may be some levels that are not in LTE with others at early times. An approximate equilibrium time among Ar II levels is several nanoseconds, so the first data set, $t1r.ufo$, from 10 ns is the most likely to be out of equilibrium. Non-LTE conditions are less likely, but still possible, in the later shots. See the the discussion subsection for more on this issue.

(2) Continuum Subtraction

We fitted and subtracted continuum levels prior to performing the emission line analysis, using a polynomial as a fitting function. When the 2nd, 4th and 10th order polynomials were used for continuum fitting, the results varied by less than 5% for most data sets. The highest discrepancy occurred at $t5r.ufo$ and there the results varied by less than 15%. We present the fitted values with the 2nd order polynomial function in the tables and figures above. The true continuum shape is unknown, and so fitting it with a polynomial probably introduces some additional uncertainties, which we cannot characterize. Partly, this is due to the fact that the "continuum" could be more accurately described as a noisy background consisting of many weak lines as well as a true physical continuum.

(3) Instrumental Broadening

The instrumentally broadened width has been measured to be between 0.4 Å and 0.5 Å in previous experiments [1]. In some initial fits, we allowed the FWHM to be freely determined by MSPECT. All data sets except $t5r.ufo$ gave a best-fit FWHM between 0.49 Å and 0.50 Å. When we examined the confidence limits on FWHM, we found that the FWHM can have virtually any value between 0.4 Å and 0.5 Å for solutions within the electron density and optical depth 90% confidence limits. Our simulations show, however, that the values derived for the temperatures and electron densities are not strongly dependent on the assumed FWHM. Despite that, the lack of precise knowledge of the instrumental FWHM may lead to some small additional systematic error. We also assume that the spectral response is Gaussian, which may not be strictly true. This is most likely to affect the levels in the wings of the line profiles, and therefore may interfere with the accuracy of the electron density determination.

(4) Plasma Temperature

The electron temperature is assumed to be 2.5 eV for all data sets. Furthermore, it is assumed to be equal to the ion temperature. The electron temperature is predicted to go up to its maximum value at early times, near 3 ns, and come down to an equilibrium value of 2 to 3 eV near 10 ns, after the beam pulse. Uncertainties in the plasma temperature probably affect the earliest data set most. Any effect of temperature uncertainty on the modeling results is most likely via the level populations. Our simulations show that assuming $T = 7$ eV for the Doppler broadening affects the derived model parameters at only the 10% level.

(5) Stark Broadening

In the current model, the Stark parameter used for each line is indicated in Table 2.1. It should be noted that not every line has an empirically determined Stark width in reference [3]. For the lines not listed there, we assumed a width of 0.32 Å at 10^{17} cm^{-3}.

Furthermore, the temperature dependence of these Stark widths is not explicitly taken into account.

(5) Gradients along line of sight

Finally, our calculations assume a constant density and temperature within the gas cell. In reality there will be gradients in these quantities along the spectrometer line of sight. Our assumption of space-independent values may constrain the integrated populations and line strengths too severely.

2.4. Modeling

We have performed some preliminary time-dependent, collisional-radiative (CR) simulations of the ion beam interactions with the argon gas cell in order to compare the predicted electron densities both with those derived from fits to the data and with those predicted by the IPROP code. We include beam impact and hot electron impact processes as well as thermal processes in these calculations. We have constructed a detailed atomic model for argon that includes over 500 levels.

The simulations assume an initial electron density equal to twice the beam ion density. They are performed with temperatures fixed at either 2 eV, 2.5 eV, or 3 eV. These models are somewhat simplified, as the temperatures as well as the beam energy are taken to be constant. In Table 2.6 we list the electron densities and optical depths from these calculations, along with those from the IPROP simulations, the Stark analysis, and our fitted MSPECT values from the optically thick model.

As shown in Table 2.6 and discussed above, the densities we derived with our optically thick model are significantly below those determined from optically thin Stark width analysis alone. In Figure 2.7 we show the time evolution of the electron density and optical depth in several CR models and compare these results to those we derived from the

Table 2.6. Comparison of Electron Density Predictions

File	Stark Only $n_e/10^{17}$ (cm^{-3})	IPROP $n_e/10^{17}$ (cm^{-3})	CR ($T = 2$ eV) $n_e/10^{17}$ (cm^{-3})	CR ($T = 3$ eV) $n_e/10^{17}$ (cm^{-3})	MSPECT $n_e/10^{17}$ (cm^{-3})
$t1r$ (10ns)	1.75	0.5	0.12	0.59	$0.50^{+0.30}_{-0.22}$
$t2r$ (13ns)	1.75	0.9	0.32	1.02	$0.49^{+0.08}_{-0.10}$
$t3r$ (16ns)	2.56	1.7	0.62	1.28	$0.68^{+0.08}_{-0.04}$
$t4r$ (19ns)	3.47	–	0.90	1.43	$1.22^{+0.12}_{-0.10}$
$t5r$ (22ns)	4.16	–	1.06	1.49	$1.75^{+0.20}_{-0.16}$

data fitting. The fitted values of n_e and τ_{4348} are consistent with the CR model results for temperatures between 2 eV and 3 eV at all but the latest data set. This temperature range is consistent with the value of 2.5 eV derived from a Boltzmann plot analysis [1]. The higher density at 22 ns could be due to contamination from impurities which are not included in our CR calculations. It might also be due to this data set having the strongest continuum level, which could lead to larger statistical errors related to the continuum fitting and subtraction.

In Figure 2.8 we show a Boltzmann plot analysis for two data sets, one taken at 6 ns and one at 18 ns. The earlier one shows significant scatter while the later one has much less scatter. This is evidence that it takes more than 6 ns for all the level populations to come into LTE. Furthermore, the quartet levels and doublet levels seem to move in concert, with the levels having the same spin coming into equilibrium with each other before the levels with different spin achieve equilibrium. Our calculations show that the doublet levels are preferentially populated by direct excitation/ionization, and that it takes some time ($\sim$ 10 ns) for the doublet populations to equilibrate with the quartet levels. In Figure 2.8 we show results from our CR models of the two Boltzmann plots. These models reproduce the trends, both of the mean temperatures and the scatter about those temperatures, that are seen in the data.

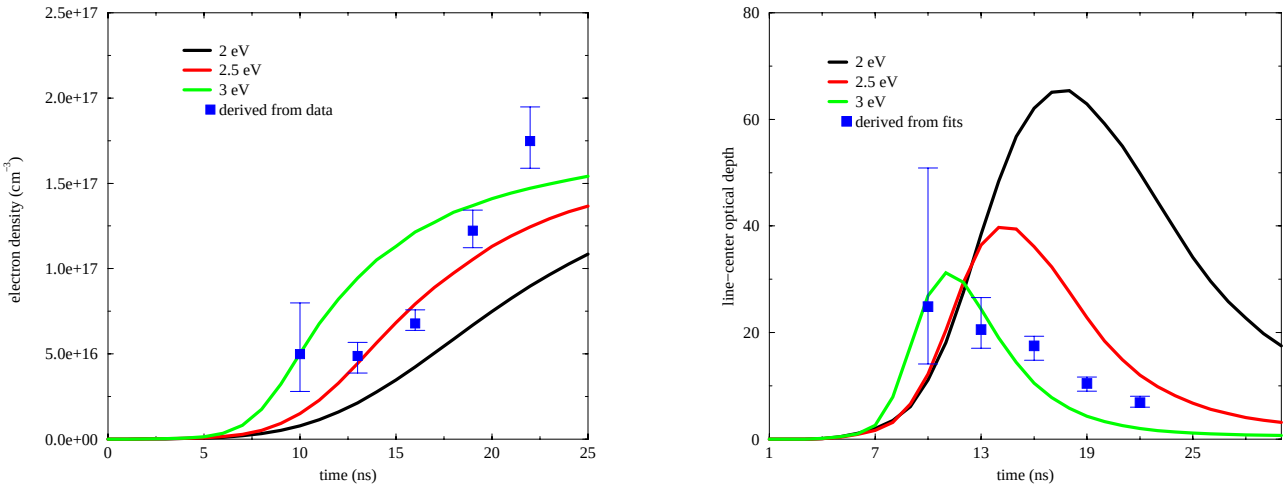

Figure 2.7. The density (left) and 4348 Å optical depth (right) values derived from the MSPECT fits are shown along with profiles from the CR calculations.

2.5. Conclusions

Now that we have shown the importance of opacity broadening, and introduced a method by which we can determine the important parameters for the argon spectra, we are able to benchmark models of the ion beam interactions with the gas cell. Whatever models are used, they must reproduce the time-dependent electron densities and line optical depths derived from the data. We have demonstrated that error evaluation and fitting multiple lines are an important part of this process.

We are now constructing more detailed atomic models of argon in order to explore the effects of hot-electron and beam ionization on the details of the optical spectra. It is hoped that this effort can be used to develop spectroscopic diagnostics of the beam properties, although initial indications are that the greatest effect of the non-thermal particles on the optical spectra are at very early times ($t < 10$ ns). Our current generation of CR models has been quite successful, however, at reproducing the electron temperature and density in

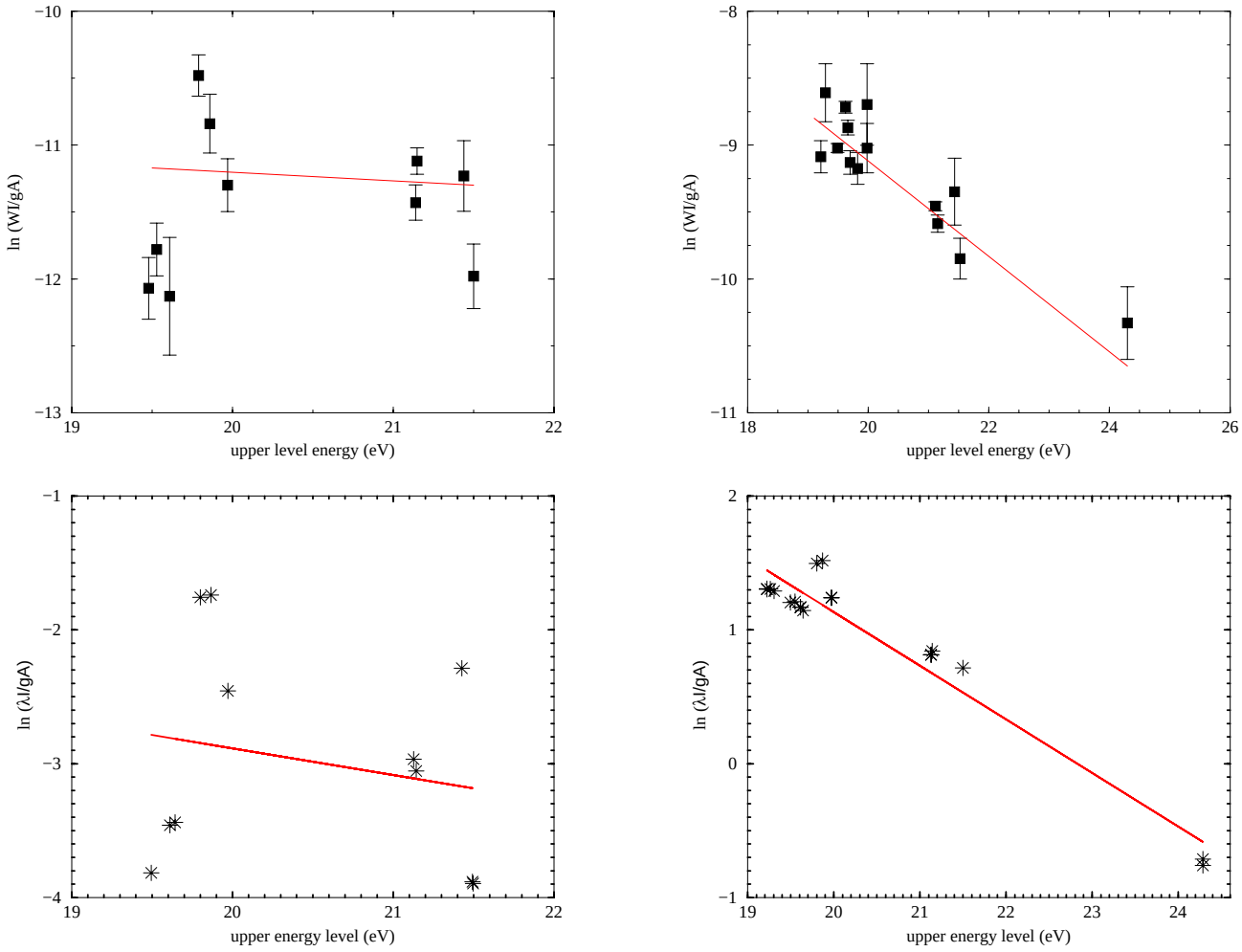

Figure 2.8. The top panels show data from 6 ns (left) and 18 ns (right). The bottom panels are from our CR models also at 6 ns and 18 ns. The red lines indicate the best-fit temperatures. In the 6 ns Boltzmann plots, the three lines with the lowest upper level energies are quartets, while the next three are doublets.

the argon gas cell. It has also reproduced the approach to equilibrium of the various Ar II levels.

References

1. Bailey, J. 1995, private communication
2. Mihalas, D. 1978, *Stellar Atmospheres*, Ch. 9, (New York: Freeman)
3. Pellerin, S., Musiol, K., & Chapelle, J. 1987, JQSRT, **57**, 377
4. Press, W. H., Flannery, B. P., Teukolsky, S. A., & Vetterling, W. T. 1991, *Numerical Recipes*, Ch. 14, (Cambridge: Cambridge University)
5. Lampton, M., Margon, B., & Bowyer, S. 1976, Astroph. Journal, **208**, 177
6. Avni, Y. 1976, Astroph. Journal, **210**, 642

3. Modeling Lithium Plasma Formation by Laser Ionization Based on Resonance Saturation (LIBORS) and Implications for Ion Beam Source Formation

Optimizing the properties of the PBFA-II ion beam depends crucially on characterizing and controlling the properties of the lithium plasma from which it is initiated. The ideal ion source for beam generation would be produced quickly and be as free as possible of thermal motions. However, it is difficult to produce a cold plasma with a large fraction of ions. In principle this requires a non-thermal process that efficiently uses the input energy to ionize neutrals while imparting as little energy as possible to the liberated ions.

Experiments have been carried out at the Sandia light-lab to test the efficacy of the LIBORS process for producing an appropriate lithium ion source on a small scale. These experiments involve irradiating a LiAg coupon with a YAG laser (fluence ≈ 0.5 J cm^{-2}) to vaporize a thin layer of the LiAg coupon. Then a dye laser tuned to the $2s - 2p$ 6708 Å transition of Li I is used to initiate the LIBORS process which produces a cold, ionized lithium plasma. In this section we discuss efforts to model the excitation and ionization dynamics of the lithium plasma using idealized zero- and one-dimensional simulations of the LIBORS process. Although these idealized models cannot fully reproduce the plasma behavior observed in the laboratory, they are a useful starting point for understanding the parameters that affect saturation, ionization, and heating.

3.1. Background

In the LIBORS process, the population of laser-excited neutrals represents a reservoir of energy which, via superelastic collisions, is transferred to the initially small population of free electrons. The electrons' interaction with the excited neutral atoms then drives the ionization. Because resonance ionization and superelastic collisions both have large cross sections, the LIBORS process can very efficiently ionize a plasma channel [1].

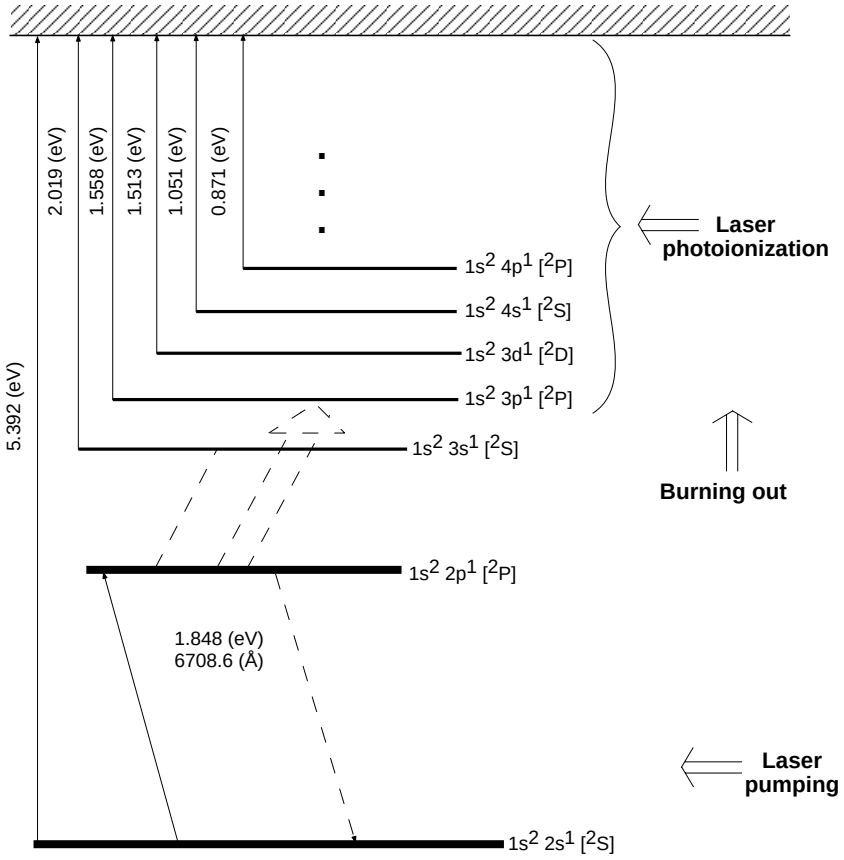

Figure 3.1. The principal energy levels of our model Li atom are shown, along with the energy level spacing.

In Figure 3.1 we show an energy level diagram of neutral lithium. The energy of the first excited level ($1s^2 2p^1(^2P)$) represents a significant fraction of the ionization potential. The laser-induced saturation quickly locks the excited state population to 3 times that of the ground state population ($g_u/g_l = 3$). This excited level now acts as a pseudo-ground-state with a reduced ionization potential. Electrons in this level are collisionally excited to higher bound levels, from which they are rapidly collisionally ionized. Because the collisional excitation (and ionization) rate is proportional to n_e there is positive feedback, so once a critical electron density is passed, the onset of ionization is sudden.

3.2. Calculations

We performed initial calculations of the LIBORS process in lithium using a zero-dimensional (single zone) model to explore the relative effects of different processes. Later, we incorporated the detailed LIBORS model into a one-dimensional calculation through a stationary slab with a density gradient. Both calculations use a lithium atomic model with 35 levels. In addition to the usual collisional and radiative processes, we considered two-photon ionization of the resonance level

$$Li(1s^2 2p^1) + 2h\nu_{12} \rightarrow Li(1s^2) + e(\epsilon)$$

and laser-induced Penning ionization

$$Li(1s^2 2p^1) + Li(1s^2 2p^1) + h\nu_{12} \rightarrow Li(1s^2 2p^1) + Li(1s^2) + e(\epsilon),$$

where $h\nu_{12}$ is the laser photon energy. We have calculated the collisional and radiative rates and energy levels ourselves, with the two-photon and Penning cross sections computed using the formalism in reference [2]. We also computed associative ionization rates [3,4], but this process proved to be unimportant in determining the ionization dynamics.

We incorporated these processes into a set of coupled, time-dependent rate equations. The code was tested by comparing ionization times for Na vapors with the results of Measures, Wizinowich, & Cardinal [5]. The very good agreement is shown in Figure 3.2.

We next calculated a series of lithium models with the zero-dimension code which explore the ion density and laser intensity parameter space. Results from one calculation are shown in Figure 3.3. Notice how strongly the electron density rises once it reaches $\sim 10^{13}$ cm^{-3}. The time of the onset of ionization depends sensitively on how quickly this electron density regime is reached. This in turn depends on the production of the seed electrons, which tends to be dominated by two-photon excitation from the $2p$ level. There is a caveat,

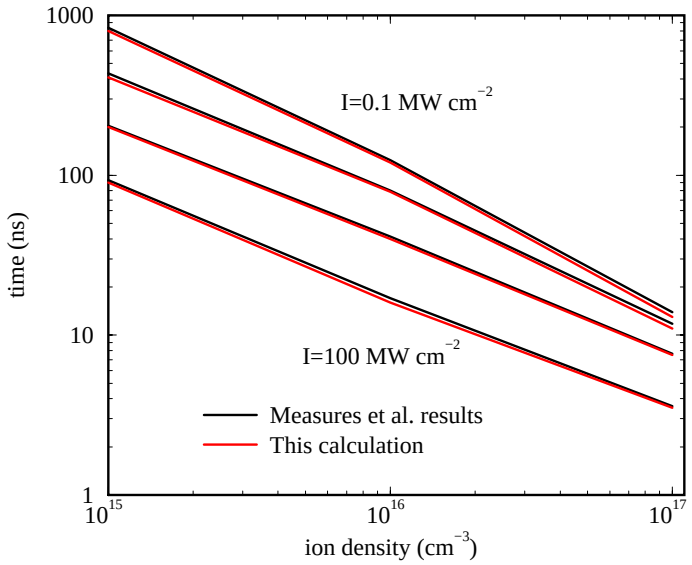

Figure 3.2. The 95% ionization times for sodium vapors with several values of laser intensity and a range of densities are shown. Our calculations show very good agreement with those of Measures et al. [5].

however. If the lithium vapor is initially ionized at all, then the free electrons present at the beginning of the calculation act as seed electrons, and the LIBORS process speeds up significantly.

The resonance transition saturates very quickly in the calculation with $n_{ion} = 10^{16}$ cm^{-3} and $I_L = 10^6$ W cm^{-2}. The speed with which the saturation occurs does, however, depend on the relative widths of the line profile and the laser profile. Figure 3.4 shows the effect on the saturation time of broadening the laser profile. However, as long as the saturation time is of order a few ns or less, its value does not significantly affect the onset of ionization.

In Figure 3.5 we show that identical saturation times can be obtained with different laser intensities, as long as the high intensity beam has a line profile that is broader than the line profile of the $2s - 2p$ transition. This figure also shows that even though saturation occurs at the same time in these two cases, in the case with the broader but more intense

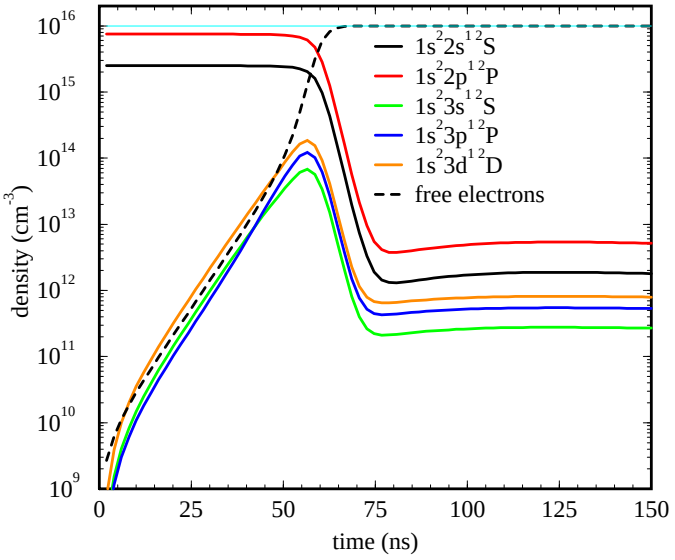

Figure 3.3. The time-histories of the level populations and electron density are shown for a zero-dimensional calculation assuming an ion density of 10^{16} cm^{-3} and a laser intensity of 10^6 W cm^{-2}.

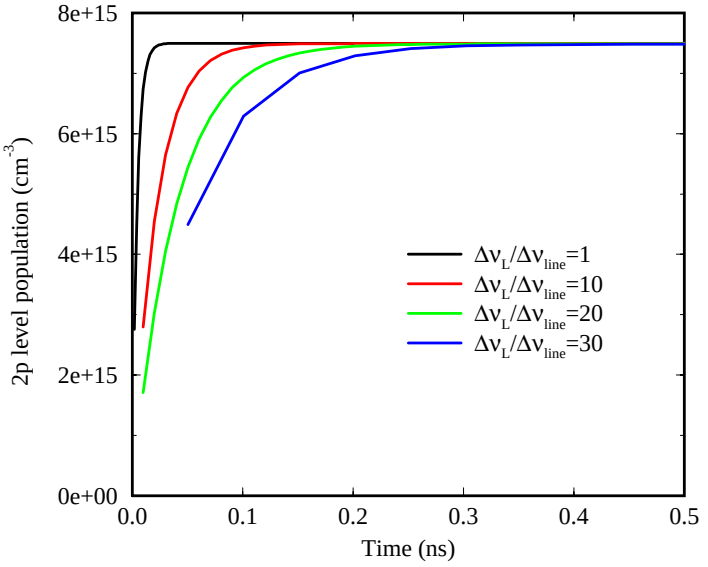

Figure 3.4. The saturation time is proportional to the laser line profile width for constant density and total laser intensity.

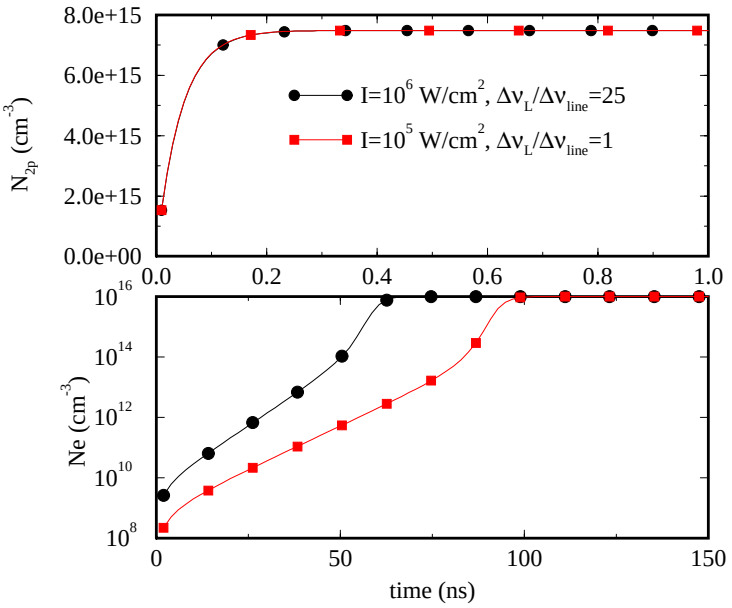

Figure 3.5. The effects of the laser profile width on the saturation time (top) and ionization time (bottom) are shown.

laser profile ionization occurs earlier. This is due to the fact that seed electron creation proceeds faster with the more intense laser as the bound-free rates are not affected by the breadth of the laser profile.

The temperature profiles for several simulations are shown in Figures 3.6 and 3.7. The red curve in Figure 3.7 corresponds to the model with the time-dependent populations shown in Figure 3.3. Note the temperature drop with the onset of ionization. This occurs because once the plasma becomes highly ionized, the superelastic collisions cannot compete with collisional cooling. When the laser intensity becomes too small, the onset of ionization is no longer rapid, as we show in Figure 3.8.

Investigations beyond these basic scalings required the one-dimensional model. It assumes a time-constant temperature and density profile (exponentially decreasing from 10^{16} at the back to 10^{15} in the front of a 1 mm long distribution of lithium). In addition to the variables solved for in the zero-dimension approximation, here we also solve for the time- (and space-) dependent laser intensity. A laser intensity profile is assumed and the radiation

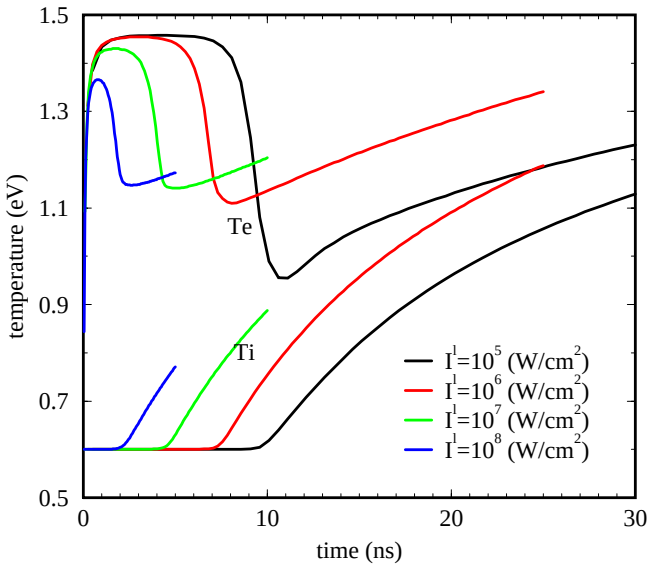

Figure 3.6. Electron and ion temperature time histories for various laser intensities and $n_i = 10^{17}$ cm^{-3}.

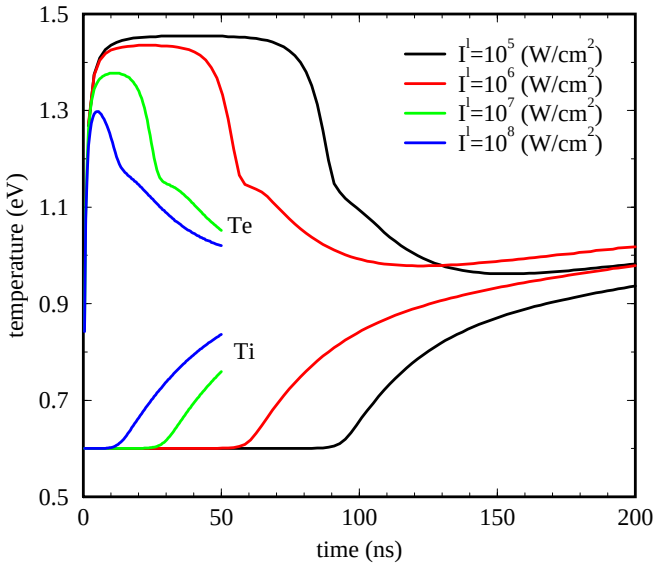

Figure 3.7. Electron and ion temperature time histories for various laser intensities and $n_i = 10^{16}$ cm^{-3}.

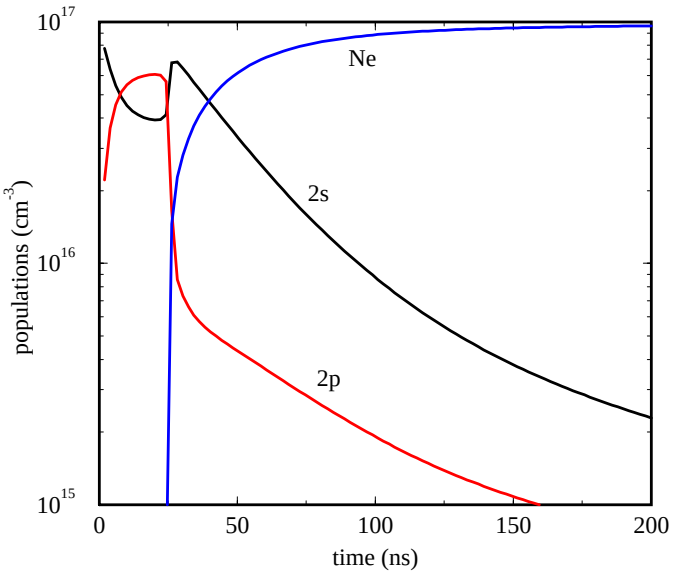

Figure 3.8. The time-dependent ground state, first excited state, and electron densities for a calculation with a low power ($I_L = 10^4$ W cm^{-2}) laser having a profile with $\Delta\nu_L/\Delta\nu_{line} = 25$ and $n_{ion} = 10^{17}$ cm^{-3}.

is transported from the low-density side of the vapor toward the high-density end. Note, though, that there is no heat flow or other communication among zones. In Figure 3.9 we show the laser intensity profile in the last zone (at the high-density end) of the calculation goes from being saturated to only marginally absorbed as the intervening lithium becomes ionized and transparent.

Although the intensity profile seen in the last zone changes with time, the inclusion of the laser transport does not alter the global behavior significantly. In Figure 3.10 we show that the $n_e(t)$ profile in the last zone is very similar to that in a zero-dimension calculation with the same density and temperature as that zone. The laser intensity in the last zone does not come close to the incident intensity for more than 20 ns in this simulation (see Figure 3.11), and this is about the same time it takes for the $2p$ level to saturate (see Figure 3.12). However, despite the delay in the onset of saturation, ionization is achieved in the back zones *before* the front zones, as can be seen in Figure 3.13. This is because the effect

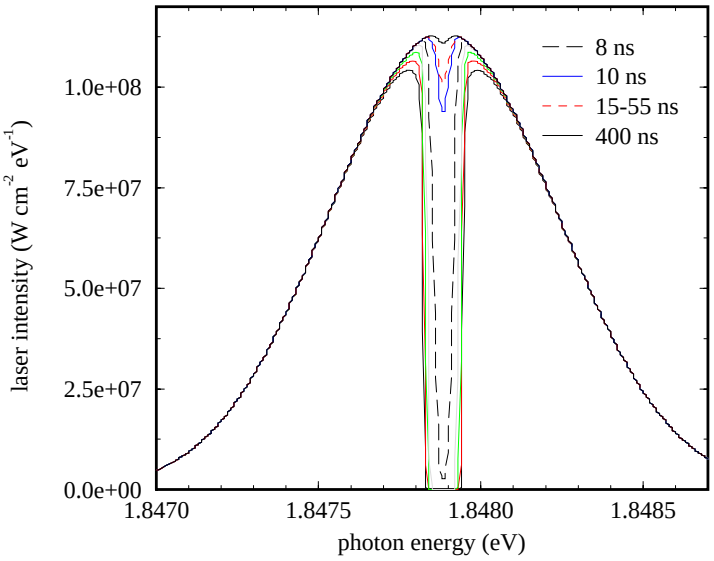

Figure 3.9. The laser profile in the last zone as a function of time. The absorption decreases with time as the intervening gas becomes highly ionized.

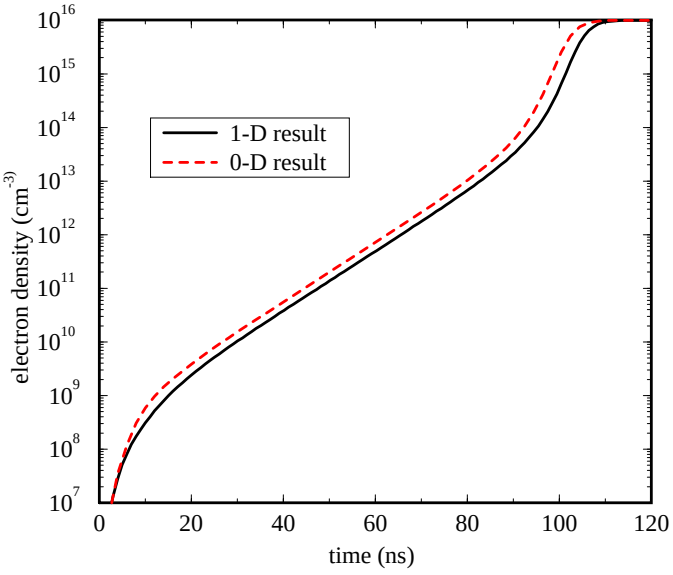

Figure 3.10. The effects of including laser transport are shown by comparing the electron density profiles of a zero-dimensional calculation with that from the last zone in a one-dimensional calculation having the same density.

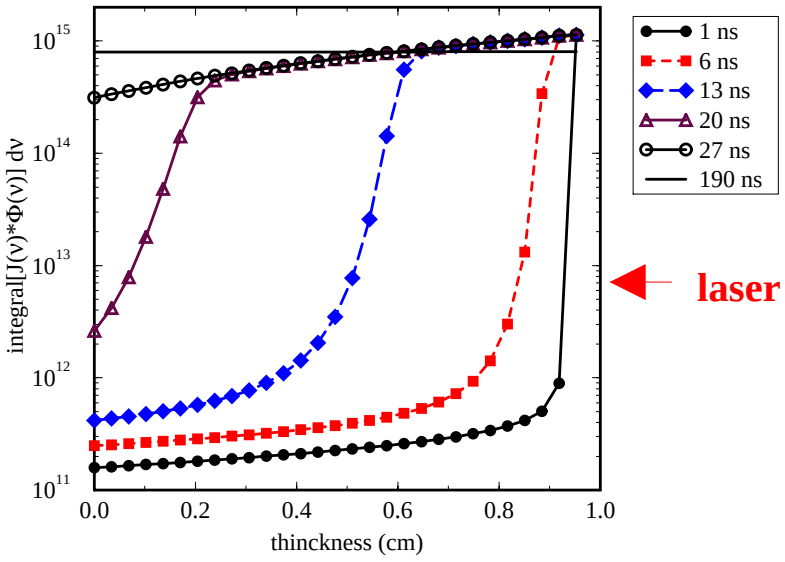

Figure 3.11. Laser intensity as a function of time and location in the vapor are shown for a model with $I_L = 10^5$ W cm^{-2} and $N_{tot} = 10^{16}$ cm^{-3}.

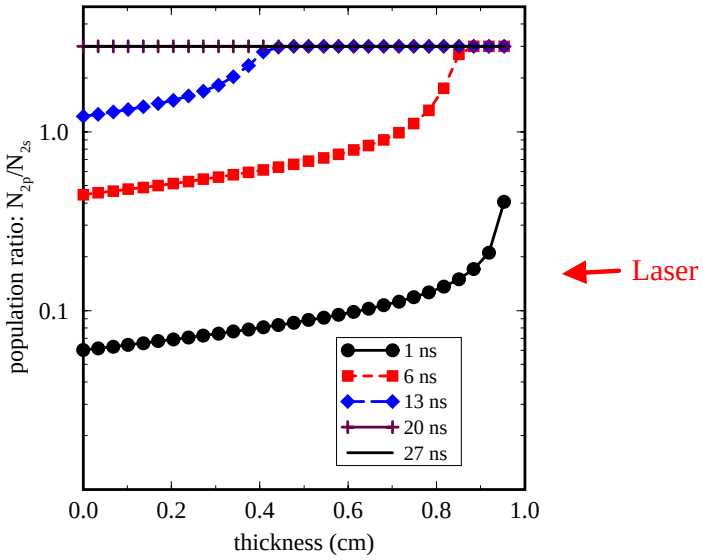

Figure 3.12. The ratio of the $2p$ to $2s$ level populations as a function of time and location is shown for the same simulation as the last figure.

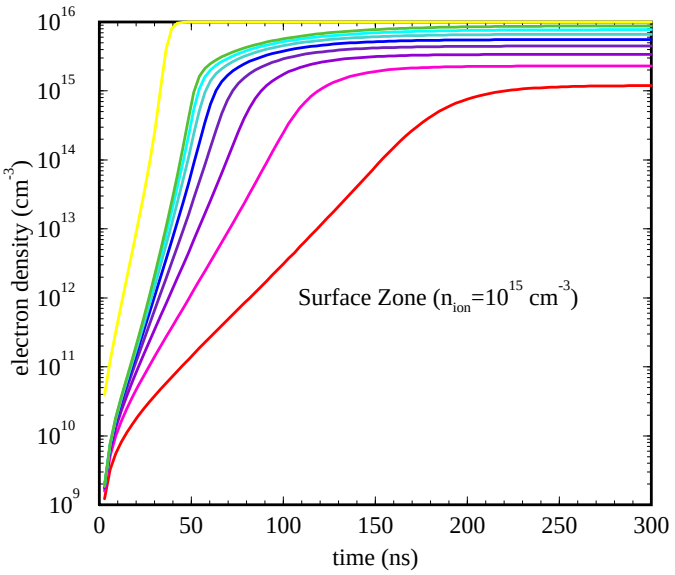

Figure 3.13. The electron density profiles for several zones of a one-dimensional calculation demonstrate that even though the laser intensity lags in the deeper zones, they ionize first.

of the additional density in the deeper zones more than compensates for the reduced laser intensity.

3.3. Discussion

We have developed a time- and space-dependent model for studying the LIBORS phenomenon in a lithium vapor with a density gradient. A very detailed atomic model and accurate atomic data have been incorporated in our calculations, which have been benchmarked against the results obtained with other codes. We find that taking the space dependence into account via its effect on the laser transport makes a small, but noticeable difference on the onset of ionization.

Our calculations show that the ionization time of the vapor is inversely proportional to the laser intensity and the vapor density, which is consistent with the results of other studies. The competing effects of density and laser intensity can interact in interesting ways.

For a density distribution that varies by a factor of ten over 1 mm, the gas in back, which sees less laser intensity than the gas in front, may still ionize first due to its higher density.

These idealized calculations have demonstrated the roles of the basic atomic processes involved in achieving burnout and have shown how some of the free parameters control the timescales involved. However, the results are sensitive to the initial conditions, especially the initial electron density. Generating the small number of required seed electrons via two-photon ionization in a fully neutral gas is relatively slow. If the lithium is initially ionized at even the 10^{-3} level, or if free electrons from the Ag or from impurities are present, then the LIBORS process may proceed much faster than our calculations indicate.

Future work could address the dependence of the ionization time on the initial seed electron population. Another effect that will probably be important in plasmas with density gradients and could be included in future calculations, is the transport of electrons among zones. As one zone becomes ionized, it will contribute seed electrons to neighboring zones. This effect will likely speed up the onset of ionization globally.

References

1. Measures, R. M., Drewell, N., & Cardinal, P. 1979, J. Appl. Phys., **50**, 2662
2. Geltman, S. 1977, J. Phys. B, **10**, 3057
3. Klucharev, A., Sepman, V., & Vujnovic, V. 1977, J. Phys. B, **10**, 715
4. de Jong, A., & van der Valk, F. 1989, J. Phys. B, **12**, L561
5. Measures, R. M., Wizinowich, P. L., & Cardinal, P. G. 1980, J. Appl. Phys., **51**, 3622

4. Radiation-Hydrodynamic and Spectral Modeling of YAG Laser Lithium Ion Source Formation

In an effort to produce a plasma optimized for the extraction of a light ion beam, a Sandia team led by Alex Filuk obtained multiple time- and space-resolved optical spectra of a moderate power YAG laser-produced plasma in the Sandia Light Lab. The laser, which had a fluence of $\lesssim 1$ J cm^{-2}, a duration of ~ 10 ns, and a spot size of 6.5 mm vaporized somewhat less than 1000 Å of a LiAg (40% to 60% by number) coupon per shot. One would expect the vapor to be heated non-uniformly by the laser, expand, and become rarefied, perhaps departing significantly from equilibrium conditions. Understanding the plasma via detailed modeling is crucial to controlling it.

We have therefore used a detailed atomic model, a one-dimensional radiation-hydrodynamic code, and a time-dependent collisional-radiative code to determine properties of the LiAg plasma. This modeling and the comparison with data allow us to explore the scaling of plasma properties with boundary and initial conditions, and to develop spectral diagnostics of the plasma. This work was motivated by the need to determine the initial conditions for the LIBORS simulations discussed in the previous section. However, as we will see, the YAG laser alone is capable of producing a significantly ionized plasma without the LIBORS process driven by the dye laser.

4.1. Hydrodynamic Modeling

All of these calculations were carried out using BUCKY-1, our one-dimensional Lagrangian radiation-hydrodynamic code [1]. It includes laser deposition, conduction, and multi-group radiation transport. The opacity of the material was calculated using a Hartree-Fock model in the context of an unresolved transition array (UTA) model for the Ag, and a detailed configuration accounting (DCA) model for the Li. For the equation of state we used the DCA/UTA models for Li and Ag at low density and a muffin tin model in the high

density regime [2]. Ion-electron temperature equilibrium was assumed in all the calculations reported here. It should be noted that due to the 1-D Lagrangian nature of our model, the 60%-40% Ag to Li ratio is constant in all zones.

We assumed a 1.06 Å Gaussian laser pulse, incident normal to the surface of the LiAg coupon. We did not model reflection, so the laser energy is completely absorbed. The laser energy is transported through the vapor, attenuated by inverse bremsstrahlung, and the remainder of the energy is deposited at the critical surface. The laser energy heats a thin layer at the surface of the coupon, which is vaporized and expands into the vacuum. Our calculations show that the conversion of laser energy to kinetic energy is efficient, with some of the laser power being converted to internal energy of the expanding plasma and a small amount being conducted back into the coupon. The density and temperature gradients in the resultant plasma are time dependent and quite strong. The laser absorption term scales as

$$\kappa \propto T^{-1.5} Z n_e^2 (1 - n_e)^{-0.5},$$

so that there is feedback between the calculated density and temperature structure and the distribution of the deposited laser energy.

Note that because of the assumed electron band structure in the LiAg model, the room temperature solid undergoes inverse bremsstrahlung in our calculation. In practice, however, at very early times before a significant quantity of plasma has formed, the laser power is deposited in a single spatial zone at the leading edge of the LiAg. Hydrodynamic motion of the LiAg is suppressed in the calculation until the temperature exceeds 0.12 eV. This mimics the energy sink of melting and vaporizing LiAg, although these processes are not treated in any detail in our model. Finally, conduction in the solid LiAg is approximated by pure Ag values [3].

Additionally, we have roughly approximated the effect of non-equilibrium ionization on the electron density by putting a minimum on the mean charge state (typically $\bar{Z}_{min} = 0.5$). This value agrees with the results of the time-dependent calculations reported in the next subsection.

Our initial calculation assumed a Gaussian laser pulse with a 8 ns FWHM and a total fluence of 0.75 J cm^{-2}. Thirty radiation groups were used and the initial solid density of the LiAg was taken to be 6.8 g cm^{-3}. Several snapshots of the temperature structure and laser deposition at early times ($t < 10$ ns) are shown in Figure 4.1. In these, and subsequent, figures the laser is incident from the right and the coupon is initially 150 μm thick.

We show temperature and density profiles at later times in the same calculation in Figure 4.2. The vapor is heated to several eV close to the coupon, expands at velocities of approximately 10 μm ns^{-1}, and becomes quite rarefied. Beyond the vicinity of the coupon surface where the density falls sharply by several orders of magnitude, the plasma density is quite flat.

We next explore the sensitivity of the computed properties of the LiAg vapor to several of the input parameters and assumptions in the calculation. This will serve both to establish the robustness of our results and to give an initial indication of the scaling of the vapor properties with experimentally controlled conditions.

The hydrodynamic calculation currently assumes LTE, which is an oversimplification for at least parts of the vapor. One consequence of this assumption is that the radiative energy losses are probably overestimated (due to the overestimation of both radiative recombination and collisional rates). In order to see how large an effect this has on the profiles, we repeated our initial calculation, but without radiative losses. The results are shown in Figure 4.3. It can be seen that suppressing radiative losses raises the temperatures only slightly and does not change the overall morphology of either the temperature or density profiles.

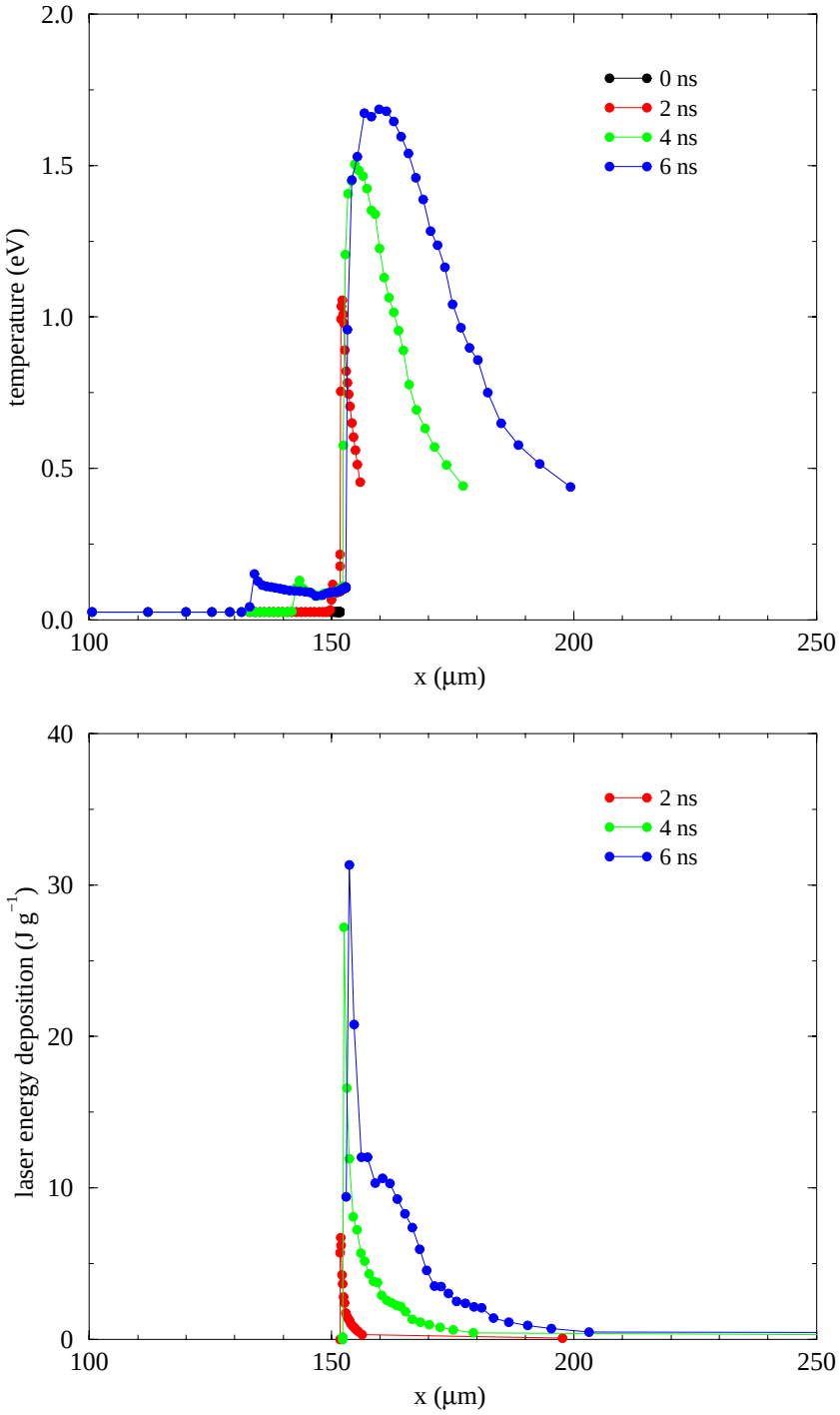

Figure 4.1. The temperature and laser deposition (per unit mass) as a function of position is shown for three early times in our hydrodynamic simulation. The front edge of the coupon is located at 150 μm. It can be seen that the greatest amount of energy is deposited near the solid/vapor interface, but that significant heating of the front of the vapor by the laser occurs as well. Note that the modest heating of the solid ($x < 150$ μm) is due to thermal conduction from the laser-heated vapor. Finally, it should be pointed out that nowhere in the vapor is the laser critical electron density reached.

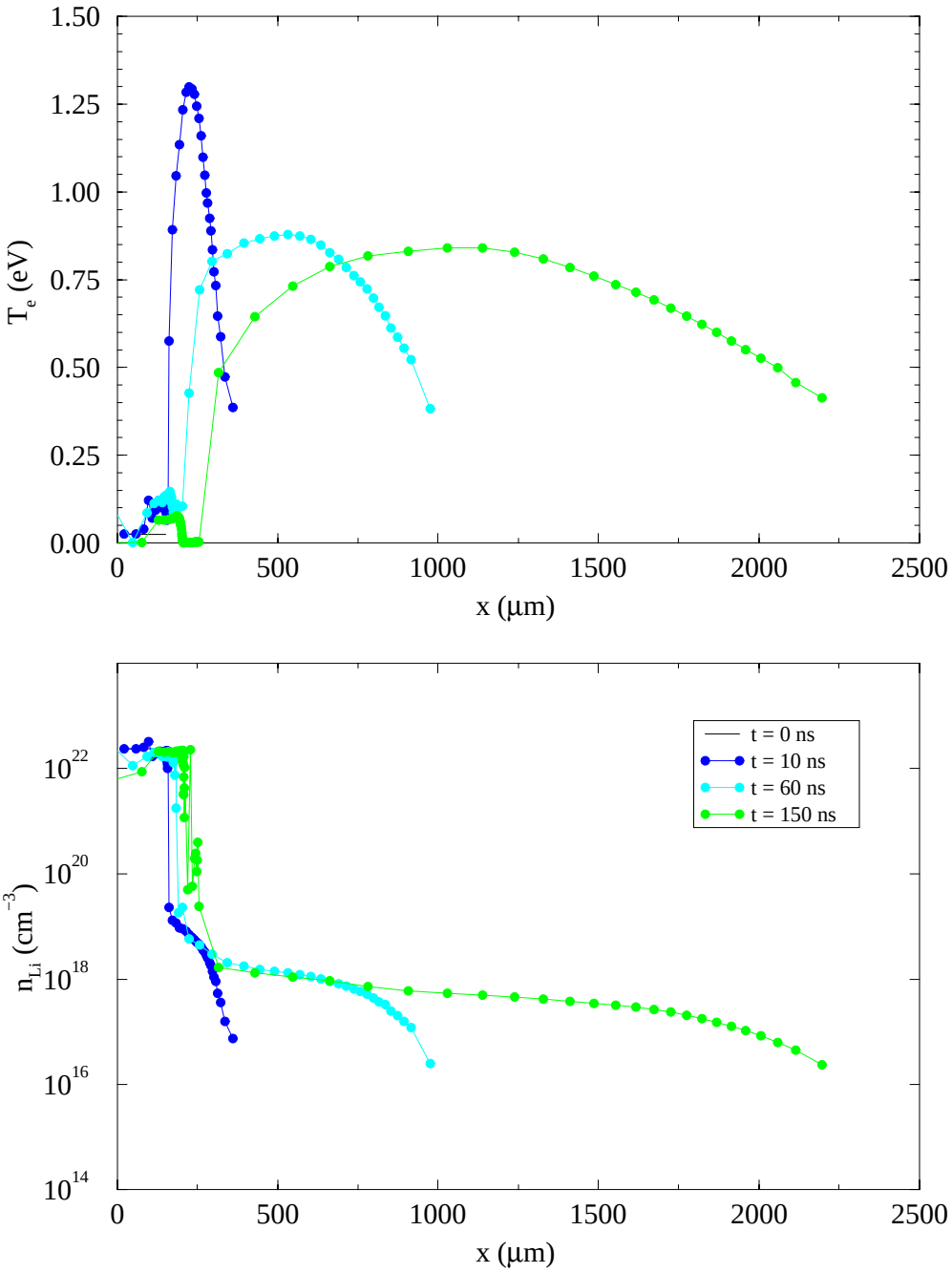

Figure 4.2. Temperatures and ion density snapshots are shown for our initial hydrodynamic simulation. Note that near the solid/vapor interface is material that has been heated above 0.12 eV, and therefore is allowed to undergo hydrodynamic motion in the calculation, but is not efficiently accelerated into the vapor region. As the calculation extends to several hundred ns, the bulk of that material stays near the interface. Resolidification is not allowed in our model, although that could very well be occurring in the actual experiments.

However, the expansion velocity does increase without radiation in the calculations, leading to a vapor that has expanded further from the coupon at any given time. Note that this increased expansion velocity leads to enhanced cooling which partially compensates for the suppression of radiative cooling, especially at late times. The temperature and density profiles under a more realistic, non-LTE treatment of radiative losses would likely be bracketed by the two cases shown in Figure 4.3.

Heat is transported from the vapor back into the solid coupon via thermal conduction. It is conceivable that the degree of heat conduction could affect the temperature and density structure of the vapor, especially if the conduction coefficient becomes quite large. In this case the coupon might act as a significant energy sink, siphoning off laser-deposited energy from the plasma. The temperature-dependent thermal conduction of the solid LiAg is treated in our calculation by solid Ag values, which, for the temperatures relevant here, are near $K = 45000$ W cm^{-2} K^{-1}. We explore the sensitivity of the computational results to the nature of the thermal conduction by performing a simulation in which we scale the value of the conduction coefficient by a factor of 2.2. The results of this simulation are shown in Figure 4.4. As expected, increasing the thermal conduction decreases the temperature, but only slightly. Furthermore, neither the density profiles nor the expansion velocity of the plasma is appreciably affected.

Finally, we explore the sensitivity of the temperature and density structure to the laser power. Unlike the conduction and radiative losses, the laser power can be easily controlled in experiments, so this scaling serves to indicate how the resultant temperature and density structure of the plasma might be adjusted. We demonstrate this scaling in Figure 4.5, where we show the profiles from our initial simulation compared with profiles from a simulation that assumed a laser pulse having only 0.5 J cm^{-2} (and the same Gaussian shape with a 8 ns FWHM).

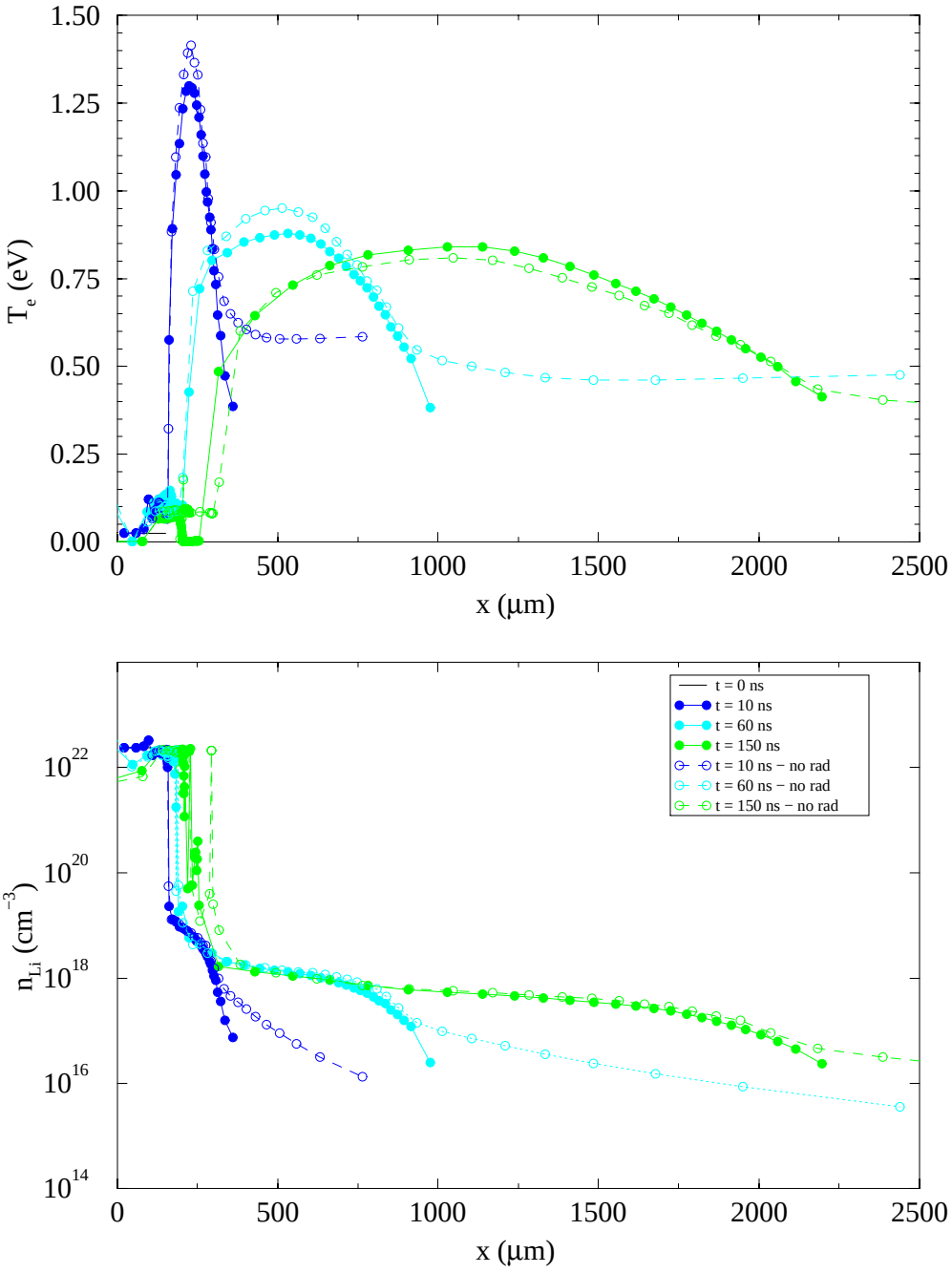

Figure 4.3. Temperatures and ion density snapshots are shown for our initial hydrodynamic simulation and also for a similar calculation in which radiative energy losses are not included.

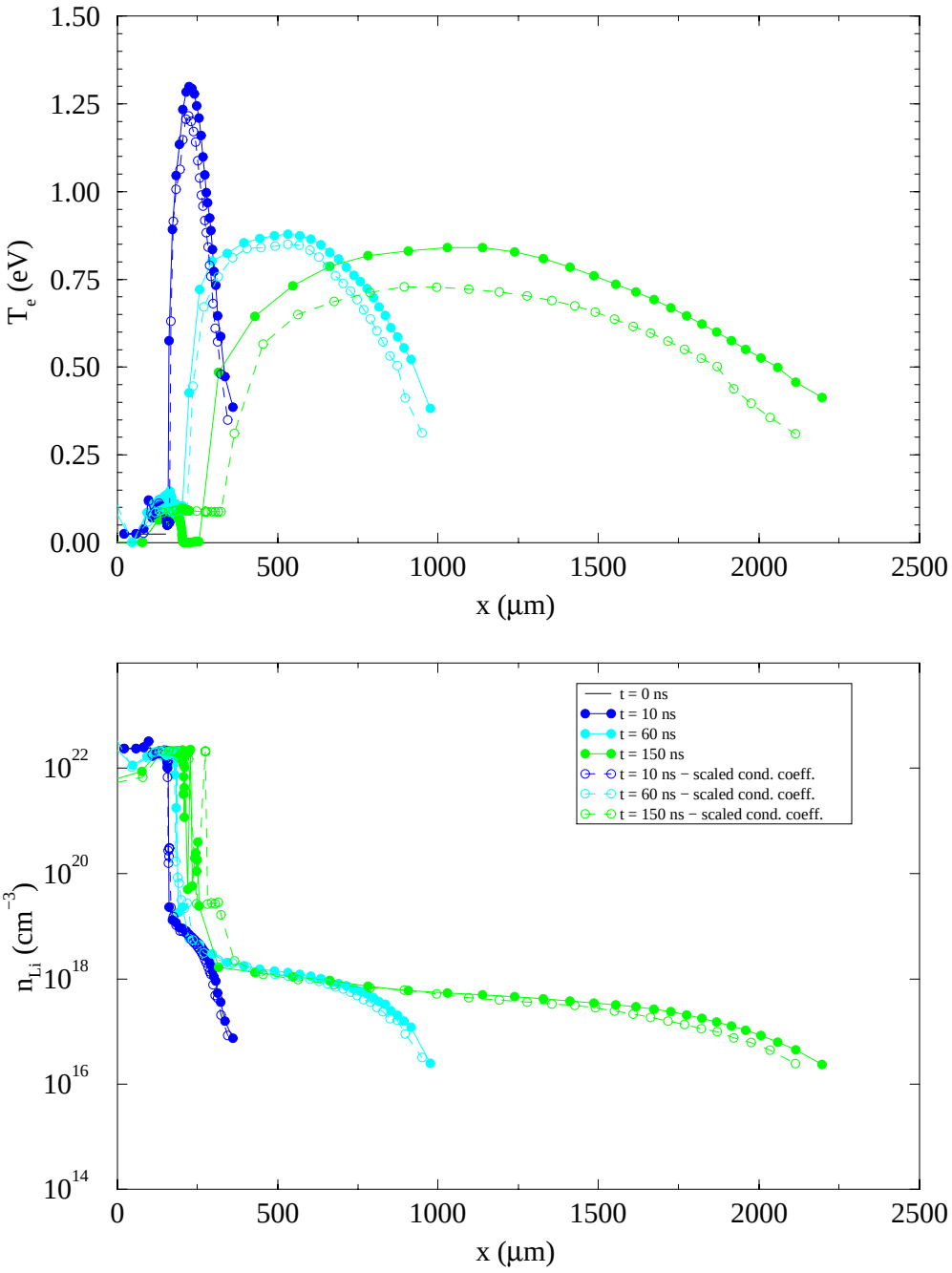

Figure 4.4. Temperatures and ion density snapshots are shown for our initial hydrodynamic simulation and also for a similar calculation in which the thermal conduction coefficient is increased by a factor of 2.2.

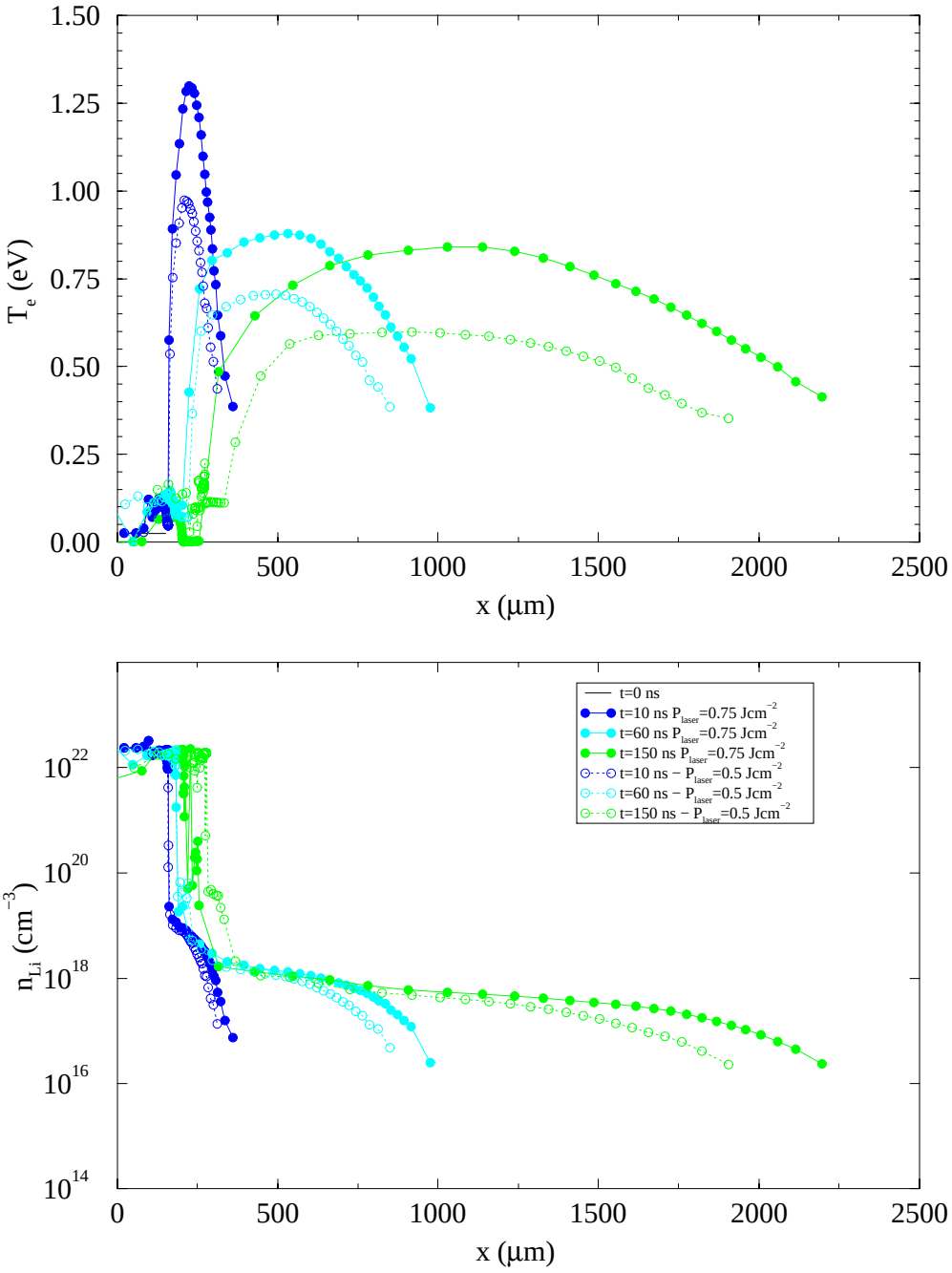

Figure 4.5. Temperatures and ion density snapshots are shown for our initial hydrodynamic simulation and also for a similar calculation in which the total laser fluence is decreased by 1/3.

Figure 4.5 shows that decreasing the laser fluence leads to a colder plasma that expands slightly slower than in the case with the full laser power. The density profiles are also similar. Interestingly, decreasing the fluence by 33% affected the total mass of ablated material negligibly. In fact, in none of the scaling explorations we report here, did the ablated mass change appreciably. It is always between 2.7×10^{-5} g cm^{-2} and 4.0×10^{-5} g cm^{-2}, which corresponds to roughly 400 Å to 600 Å of solid LiAg. Thus neither the total incident energy nor the rate at which energy is lost by the plasma strongly affects the amount of material in the plasma. They have a much stronger effect on the thermal and kinetic properties of the plasma.

4.2. Collisional-Radiative Modeling

For much of the plasma, LTE is probably a poor assumption due to the low densities. Furthermore, statistical equilibrium may not hold if the densities are low enough and the gradients strong enough. Thus, in order to calculate the level populations and spectrum one needs to compute a time dependent collisional-radiative model [4]. We do this by following the time-dependent temperature and density of an individual Lagrangian cell in the hydrodynamic calculation. For this cell we integrate the rate equations forward in time. By repeating this process for a series of computational cells, we can build up a series of time-dependent spectra at selected lines of sight perpendicular to the expansion direction. In Figure 4.6 we show the temperature and density of three representative computational cells as a function of time. Profiles such as these are used as input for the time-dependent collisional-radiative modeling.

Our model includes 44 levels of lithium and 40 levels of silver, most of which have been checked against experimental data. We also include between 0.1% and 5% hydrogen (9 levels) in the model to account for the LiH impurities on the coupon surface. The atomic models use the Hartree-Fock method in the intermediate coupling approximation, and assume an isolated atom. Due to the isolated atom assumption, the enhancement of the Li I $2p-3p$

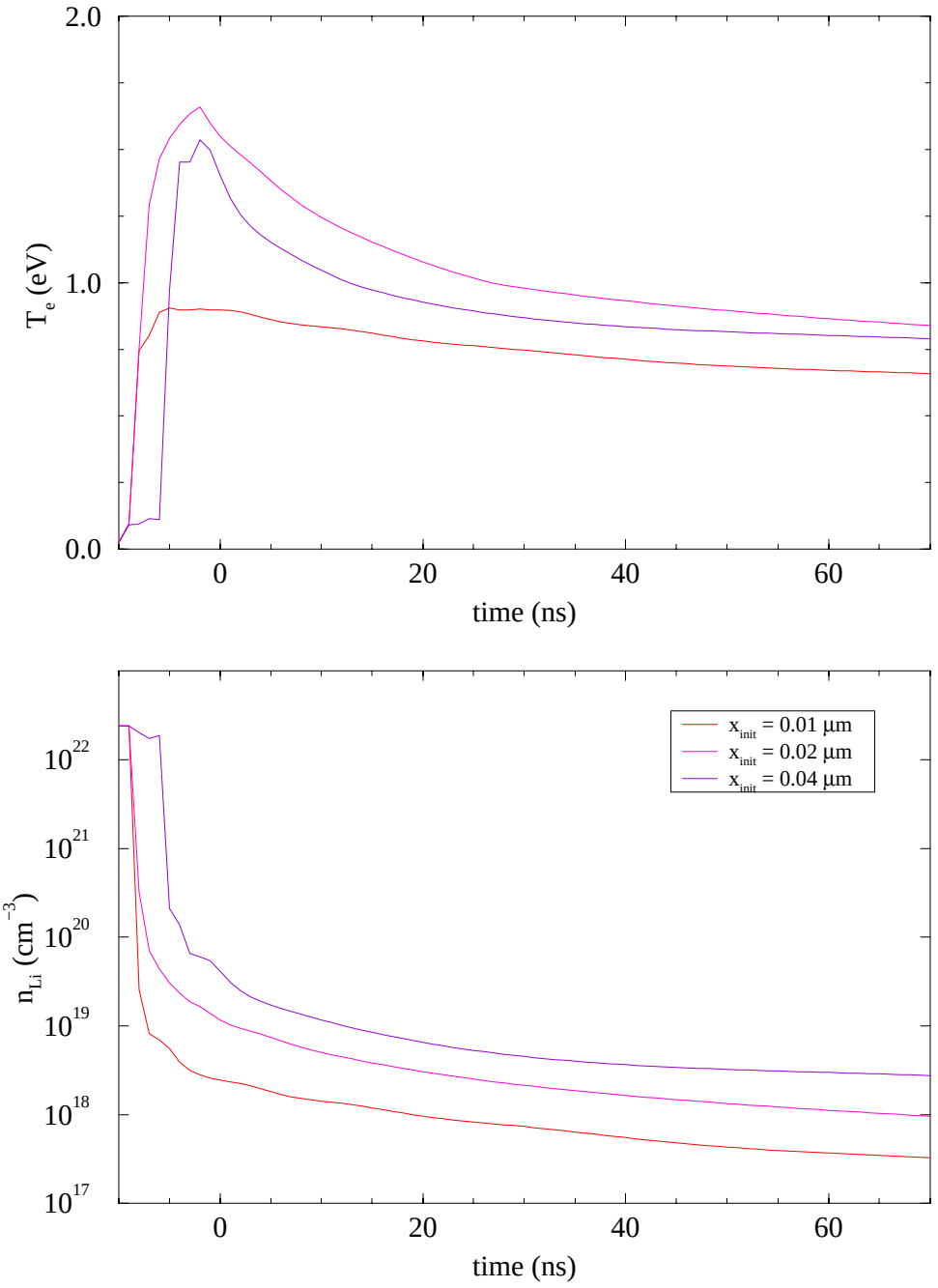

Figure 4.6. Temperatures and Li atomic density time-profiles are shown for three computational cells near the surface of the LiAg coupon. Note the rapid decline in density at the time the peak temperature has been reached.

forbidden line is not included in our calculations. Also the Stark shifts observed in some lithium lines are not included. We use Voigt profiles for the spectral synthesis, with Stark widths calculated according to Griem's semi-empirical formula [5],

$$W = 3.87 \times 10^{-7} n_e T_e^{-1/2} (r_i \bar{g}_i + r_f \bar{g}_f),$$

where W is the angular frequency expressed in Hz, $\bar{g}_i$ and $\bar{g}_f$ are the gaunt factors for the initial and final states, and r_i and r_f are the mean squared electron radii, which are taken from our Hartree-Fock calculations of atomic structure. Finally, we assume that the plume has a transverse thickness of 6.5 mm.

In this report, we compare our simulation results to light-lab spectra taken side-on to the plume at 150 ns (LAPIS shot 9-3-97). In Figure 4.7 we show calculated spectra at 375, 625, 875, 1125, 1375, and 1625 μm from the coupon surface, and in Figure 4.8 we show the corresponding LAPIS data set. The overall properties of these simulated spectra are similar to those seen in the data. Specifically, the intensity peaks around 1 mm; several lines are quite optically thick, coming up to the blackbody level; and two Ag I $5s - 5d$ lines are strong. There are, however, some important differences: the forbidden Li I $2p - 3p$ line is very weak (because state mixing is not included in our model), there are no significant hydrogen features in the model, and the continuum is stronger in the model than in the data.

In Table 4.1 we show some figures of merit for our time-dependent spectral simulation, including optical depths, level populations, and ionization fractions. Both the ionization fractions and level populations indicate that the plasma is far from LTE, especially in the cooler outer regions of the plume, where the temperatures are very low but many ions still exist. Material, as it is ablated from the solid LiAg, is rapidly heated and ionized, and then becomes quite rarefied. With particle densities well below 10^{20} cm^{-3}, recombination timescales are longer than dynamical timescales and the Li and Ag are overionized and overexcited for the local thermal properties of the plasma. The population of electrons in the

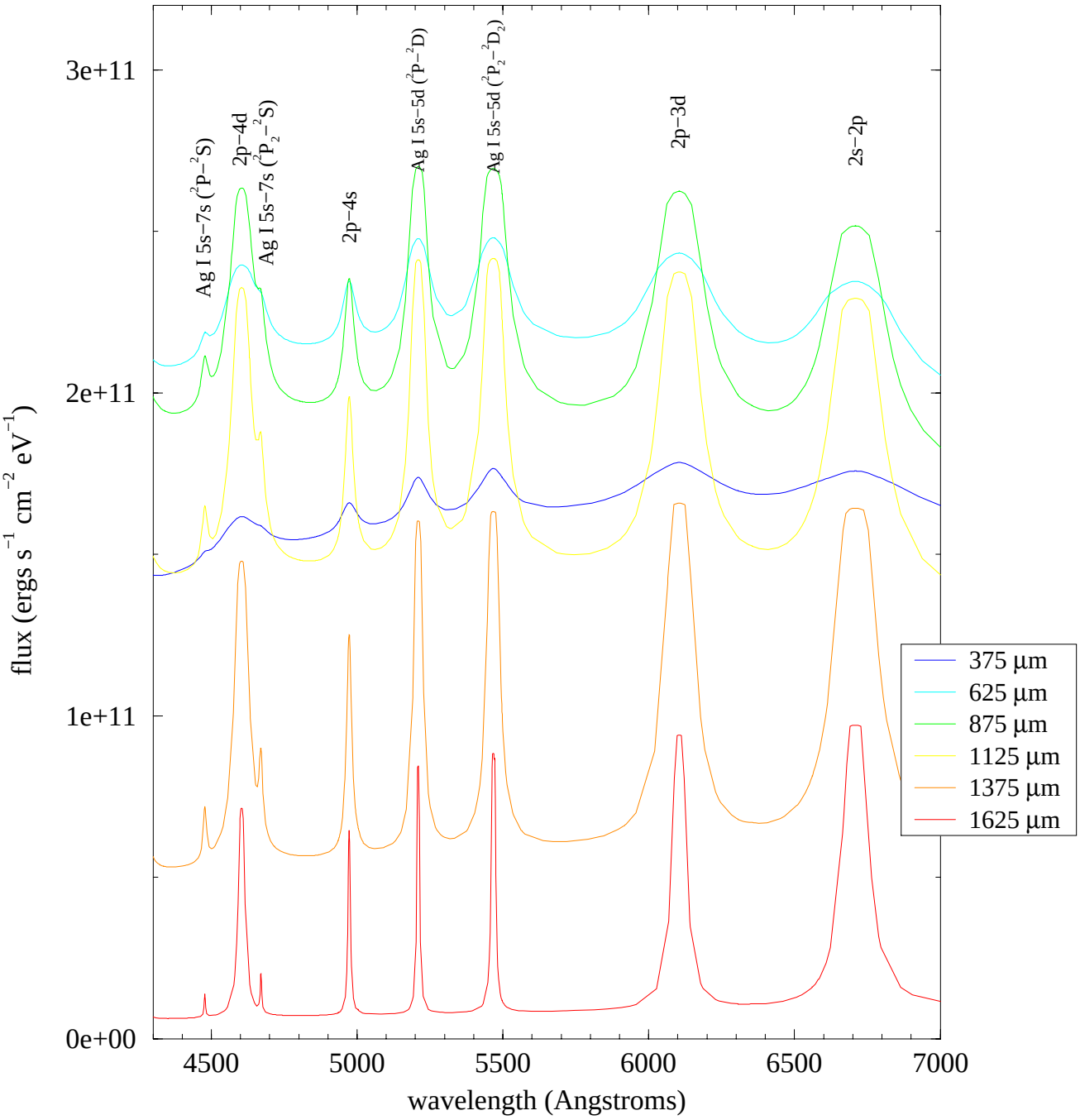

Figure 4.7. Simulated spectra from a side-on view of the LiAg plume at 150 ns and at a series of distances from the coupon.

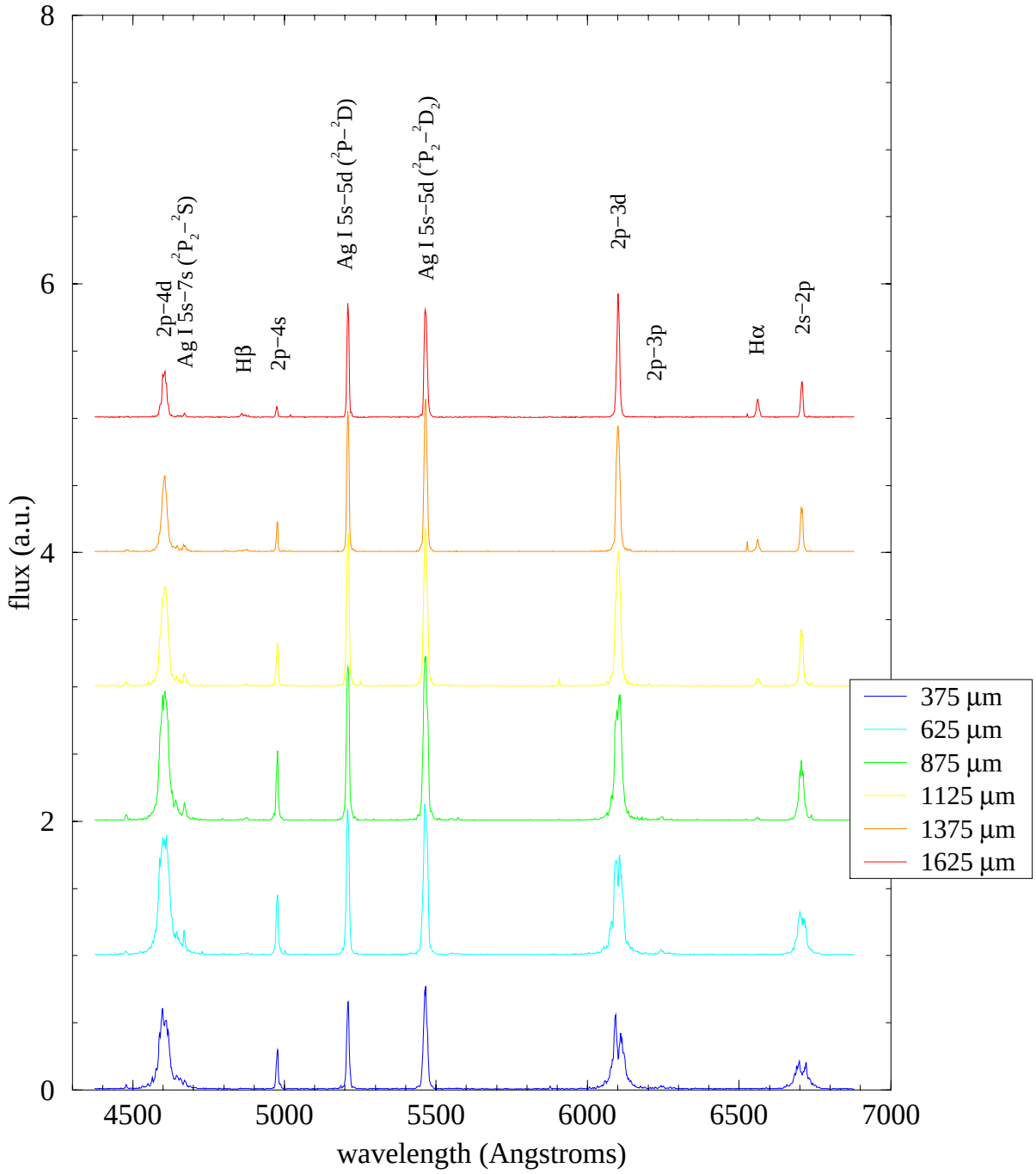

Figure 4.8. Spectral data from LAPIS shot 9-3-97, taken at 150 ns side-on to the LiAg plume, at a series of distances from the coupon corresponding to the calculations shown in the previous figure. Note that the data sets have been scaled, each by a unit, from the previous one. There is no evidence for continuum emission.

$3d$ and $4d$ states of Li I is many orders of magnitude above the LTE values, even for regions of the plasma significantly closer than 1 mm to the coupon.

Table 4.1. Time-dependent Collisional-Radiative Results

Distance	Li I Populations[a]				X_{ion}		Optical Depths[b]			
(μm)	$2s$	$2p$	$3d$	$4d$	Li I/Li II	Ag I/Ag II	$2p-4d$ 4604 Å	Ag I $5s-5d$ 5209 Å	$2p-3d$ 6104 Å	$2s-2p$ 6709 Å
375	0.33	0.33	0.0054	0.0021	0.52/0.48	0.89/0.11	22	49	337	6030
875	0.33	0.13	0.0043	0.0019	0.29/0.71	0.62/0.38	7	32	100	1290
1375	0.33	0.22	0.0032	0.0012	0.34/0.66	0.80/0.20	9	26	144	2750

[a] The level populations as a fraction of the total number of Li ions. Note that the calculated populations for the n=2 states are close to the LTE values, while those for the n=3,4 states are orders of magnitude above the LTE values.
[b] Line center optical depths.

The line center optical depths, while large, are not as large as might be expected given that the total lithium particle densities are never far below 10^{18} cm^{-3}. Indeed, dye laser transmission diagnostics indicate that neutral lithium densities in the plasma are of order 10^{16} cm^{-3} [6], while calculations of combined Stark- and opacity-broadened line profiles indicate that these low densities imply optical depths on par with those we calculate here for the higher densities [7]. This discrepancy may be reconciled by the fact that if our calculations overestimate the electron densities then they also overestimate the Stark widths of the lines, and therefore underestimate the line-center optical depths. However, this still leaves unresolved the value of plasma particle density, which is significantly larger in our calculations than is implied by both the Li I line widths and the relatively weak observed continuum. It is possible that our calculations significantly overestimate the total mass of vaporized LiAg because we assume full absorption of the laser pulse, while there are indications that, at least at early times, much of the laser energy is reflected.

The lack of Hα and Hβ in our model spectra, despite the inclusion of a significant amount of H in the calculation, is somewhat puzzling. However, we should point out that the temperature of any given computational cell rarely exceeds 2 eV. Hydrogen has a significantly higher ionization potential than does either Li or Ag, and so it is not surprising that, in our

calculations, the upper levels of these Balmer series transitions do not get populated. It is possible that we are underestimating the peak temperatures in the hydrodynamic calculation. It is also possible that charge exchange leads to the ionization of hydrogen and the Balmer lines are produced upon recombination of the hydrogen.

Finally, we should point out that the one-dimensional nature of the simulations prevents us from modeling hot spots (and corresponding density inhomogeneities) and the lateral expansion of the plasma. In the experiment, lateral expansion of the plume will lead to temperature and density gradients along the line of sight to the spectrometer, which would affect the optical depths and the line profiles.

4.3. Conclusions and Directions for Future Work

Although our model is rudimentary in many respects, it provides a relatively good reproduction of the qualitative trends in the data, with the major discrepancies being the high densities, which are manifest as the excess free-free continuum, and the lack of forbidden and hydrogen emission in our spectral model. The major results of the modeling are as follows: The total ablated material is insensitive to most adjustable parameters; most of the laser energy goes into kinetic energy of the plume; non-equilibrium effects are important; line opacity effects are important. Additionally, the silver lines seen in the optical spectra may prove useful as temperature diagnostics.

Future work will include the effects of state-mixing and Stark shifts, which should lead to enhanced $2p - 3p$ forbidden emission. We will also incorporate a better model, or preferably experimental data, of the Stark widths of the lithium lines. The future work will also include a model of laser reflectivity at early times. With significantly less energy deposited in the coupon in a narrower pulse, it is possible that the ablated mass will be reduced and therefore the predicted electron densities and free-free continuum may also come more into line with the data. Charge exchange will also be explored in future

modeling. Finally, we plan on incorporating the time-dependent CR calculation within the hydrodynamic calculation in order to get a more realistic determination of the electron density (and thus EOS and laser deposition) and radiative losses into the computation.

References

1. MacFarlane, J. J., Moses, G. A., & Peterson, R. R. 1995, UWFDM-984
2. Wang, P. 1993, UWFDM-933
3. Powell, R. W., Ho, C. Y., & Liley, P. E., NSRDS-NBS 8
4. MacFarlane, J. J., Peterson, R. R., & Moses, G. A. 1995, UWFDM-1050
5. Hey, J. D. 1977, JQSRT, **17**, 729
6. Vesey, R. 1998, private communication
7. Bailey, J. 1998, private communication

Acknowledgment

Support for this work has been provided by the U.S. Department of Energy.